Master's Thesis

Master Earth, Surface and Water

Utrecht University

Evaluation of different approaches to modelling dynamic unsaturated fluid flow conditions in hydrophilic nonwoven fibrous layers

Ruben Boelens

Utrecht, December 2018

Author: **Ruben Boelens**

Student number: **4004507**

University supervisor:

prof. dr. ir. Majid Hassanizadeh (S.M.Hassanizadeh@uu.nl)

second supervisor:

Amir Hossein Tavangarrad, MSc (A.H.Tavangarrad@uu.nl)

30 ECTS

Earth Surface and Water

Faculty of Geosciences, Utrecht University

Utrecht, December 2018

Abstract

This study investigates the applicability of statically measured hydraulic properties of a compressed thin nonwoven fibrous layer, to predict unsaturated dynamic fluid flow conditions. The autoporosimetry technique was used to perform both quasi-static and dynamic inflow and outflow experiments. In the quasi-static experiments, air pressure is increased or decreased in small increments to identify static water retention curve parameters. During dynamic experiments, one large pressure step was applied, after which the saturation of the fabric sample through time was recorded. Three different types of models to simulate the dynamic experiments have been examined: a Richards equation-based model, a two-phase flow Darcy-based model, and a Reduced Continua Model (RCM). Traditional continuum-scale Richards and Darcy based models are in good agreement with laboratory data for fabric layers without surficial bonding patterns. However, the initial moment of inflow experiments had a clear time delay comparing to continuum-scale modeling results for materials with bonding patterns. Including the effect of dynamic capillarity and modification of the relative permeability function, within the 2D axisymmetric Darcy model, yields satisfactory results. However, these modifications to the model are arbitrary and inconsistent. A recently developed model for modeling multiphase flow through a stack of thin porous layers, called the RCM, is employed to account for the effect of interlayer pore space between the thin fabric and membrane. The interlayer space effect is accounted for within the mass transfer function of the RCM. It was found that the interlayer space effect can explain the mentioned delay of initial wetting. Perfect match between experimental and modeling results are obtained, after considering a low interface transfer rate coefficient in the RCM simulations of the fabric layers with surficial bonding patterns. The dynamic outflow experiments are modeled with the same mass transfer functions as the inflow experiments, also yielding results that are in good agreement with experimental outflow data. This study shows that the RCM is more accurate and computationally more affordable compared to traditional continuum-scale models, when it comes to modeling flow through a stack of thin porous layers.

Acknowledgements

I would like to thank prof. dr. ir. Majid Hassanizadeh and Amir Hossein Tavangarrad for the opportunity they gave me to contribute in this interesting research project during which I learned a lot. Amirs door was always open to me, and the numerous discussions we have had were of great help. It is important to note here that the experiments discussed in this study have been performed by Amir (Tavangarrad, 2019). The modelling part of this study has been performed by me.

Table of Contents

List of Figures

List of Tables

1 Introduction

Thin nonwoven fabrics have a wide range of applications. Examples are hygiene products, filters, and fuel cells. The performances of fibrous products depend primarily on the hydraulic characteristics of the used thin fibrous layer. In order to optimize the performance of fibrous products, it is crucial to gain knowledge on the hydraulic properties of thin fabrics. One of such hydraulic properties is the capillary pressure-saturation relationship, $P_c(S)$, during fluid flow in a thin porous layer under unsaturated conditions. Research focusing on measurements of this $P_c(S)$ relationship predominantly concern gas diffusion layers (GDL) of polymer electrolyte fuel cells (PEFC) (Gostick et al., 2006, 2008; Nguyen et al., 2008), as well as hydrophilic fabrics used in medical and hygienic absorbent products (Landeryou et al., 2005; Tavangarrad et al., 2018).

The hydrological behavior of thin porous layers differs from that of thicker porous media. This is often so because physical processes of fluid flow that are negligible in a thick porous media, may become dominant in a thin medium (Prat & Agaësse, 2015). For example, gravity forces can be expected to be negligible in thin porous medium. As a result, the competition between viscous forces and capillary forces, become even more dominant.

In order to understanding the behavior of unsaturated fluid flow through a thin porous media, modeling research has been conducted with both continuum-scale models (Landeryou et al., 2005; Qin et al., 2012; Ye & Nguyen, 2007) and pore scale models (Ashari & Tafreshi, 2009; Aslannejad & Hassanizadeh, 2017; Jaganathan et al., 2009). 3D Pore-scale modeling has been used to determine the capillary pressure-saturation curve of thin fibrous paper (Aslannejad & Hassanizadeh, 2017). Ashari & Tafreshi (2009) simulated the quasi-static distribution of water and air for an arbitrary capillary pressure using 3D microstructures resembling the internal geometry of fibrous sheets. They developed general mathematical relationships for capillary pressure and relative permeability in terms of saturation for fibrous sheets.

Traditional continuum-scale Darcy-based models have been used to simulate water infiltration and drainage (Landeryou et al., 2005; Qin et al., 2012; Ye & Nguyen, 2007) . Landeryou et al. (2005) studied the in-plane infiltration in horizontal and inclined thin fibrous sheets experimentally and numerically, using a Richards equation-based model. Ye & Nguyen (2007) developed a 3D two-phase transport model to predict water saturation in PEFCs. They incorporated experimentally measured capillary pressure functions in their model.

Rebai and Prat (2009) used traditional continuum models and a pore network model to predict the water distribution across a thin layer. They stated that traditional continuum-scale modeling cannot be relied on to compute the water distribution along the thickness of thin layers, because the pore size is comparable to the thickness. Qin & Hassanizadeh (2014) also indicated that the applicability of continuum-scale Darcy-based models to these extremely thin porous layers, is very questionable. Continuum description of a multiphase porous medium at the Darcy scale implies that the relevant physical quantities defined at a given point, represent averages taken over a pore-scale representative elementary volume (REV) associated with that point. The size of the REV must be significantly larger than the pore-scale dimensions (Bear, 1972). For thin porous layers this is often not the case. If the layer thickness is less than one order of magnitude larger than the mean pore size, the REV length scale requirements are not satisfied (Qin & Hassanizadeh, 2014). Such layers are defined as ‘physically thin porous layers’. Layers for which the REV scale requirements are satisfied, but for which the in-plane dimension is much larger than the through-plane dimension (thickness), are defined as ‘geometrically thin porous layers’.

To overcome the shortcomings in the traditional Darcy-based continuum-scale models when it comes to the simulation of multiphase flow through a stack of thin porous layers, Qin & Hassanizadeh (2014) developed the Reduced Continua Model (RCM). In this modeling approach, each layer is modeled as a

2D domain with governing equations formulated in terms of thickness-averaged properties. The inter layer interactions are accounted for by a transfer term of mass, heat and momentum. Qin & Hassanizadeh (2015) used the RCM to model liquid water flooding in the GDL and micro porous layer (MPL) of a PEFC. They found that the RCM simulates similar fluid flow dynamics in the MPL (which is a geometrically thin porous layer), but also simulates a lower steady-state water saturation in the GDL (which is a physically thin porous layer), when compared to simulations with a Richards equation-based model. Tavangarrad et al. (2018) monitored the change of saturation during the dynamic drainage of a thin fibrous layer by placing a fully saturated layer of nonwoven fabric on top of a dry layer. Both a Richards equation-based model and a RCM were used to simulate the experiment. The traditional Richards equation-based model could not simulate the experimental results satisfactory. Only after including a dynamic capillarity term, as described by Hassanizadeh & Gray (1993), satisfactory results were obtained. The RCM simulations were in good agreement with experimental results, also without the addition of a dynamic capillarity term. Moreover, the computational efforts of the RCM are significantly lower than those of traditional continuum-scale models (Qin & Hassanizadeh, 2015; Tavangarrad et al., 2018).

Studies on two-phase flow behavior in granular soils have indicated that capillary pressure-saturation relationships depend on the fluid flow dynamics (Hassanizadeh & Gray, 1993; Beliav & Hassanizadeh, 2001; Hassanizadeh et al., 1997). It has been investigated how soil retention curves that are measured under static conditions can be applied to simulate transient one step inflow/outflow experiments. It was found that the differences between statically or dynamically measured Pc(S) curves depend on the rate of change of saturation. Most studies that include dynamic effects concern research on granular soils. To the best of our knowledge, no studies exist on how capillary pressure-saturation function of nonwoven fabric may change during dynamic flow conditions.

In this study, inflow and outflow experiments have been carried out to investigate the applicability of statically measured hydraulic properties of a compressed thin nonwoven fibrous layer to simulate dynamic fluid flow conditions. An autoporosimetry technique developed by Miller and Tyomkin (1994) was used to measure both the quasi-static and dynamic inflow/outflow water retention curve. In the quasi-static experiments, the pressure gradient was changed in a stepwise manner to measure the static water retention parameters after reaching equilibrium. For the dynamic experiments one large, almost instantaneous, pressure step was applied. The statically measured hydraulic properties were then used to model the dynamic fluid flow conditions. Three different types of models have been examined: a) a Richards equation-based model; b) a two-phase flow Darcy-based model; and c) a Reduced Continua Model (RCM).

2 Methodology

2.1 Experimental setup and materials

2.1.1 Materials

Six hydrophilic thin nonwoven fibrous layers, of which two polypropylene layers, two polyester layers, a cellulose layer and a glass fiber layer, were used for this study. Properties of these layers, under 0.3 psi overburden pressure, are shown in Table 1. Porosities were calculated based on maximum water uptake of each layer. Permeabilities were measured using the falling head method. Permeability values vary within a range of two orders of magnitude.

The layers were named based on the type of material and their basis weight. The polypropylene PP-25 layer was thermally bonded with a lozenge bonding pattern. The PP-10 was spunbonded in a circular pattern. Surfactant was added to the two polypropylene layers to make them hydrophilic. The polyester P-86 layer was bonded in a circular pattern in some regions. Fig. 1a and 1c illustrate how this bonding process has impacted the surface structure. PP-25, PP-10, and P-86 are three fibrous materials for which the surficial structure has been affected by a bonding process. The polyester P-60, cellulosic C-155, and

glass fiber G-120 layers have been subjected to other bonding processes which did not alter their surficial structure (Fig. 1b). The membrane that was used underneath the fibrous layers in the experimental setup was made of cellulosic esters. This membrane had a porosity of 0.82, and a permeability of 6.1e-14 m^2.

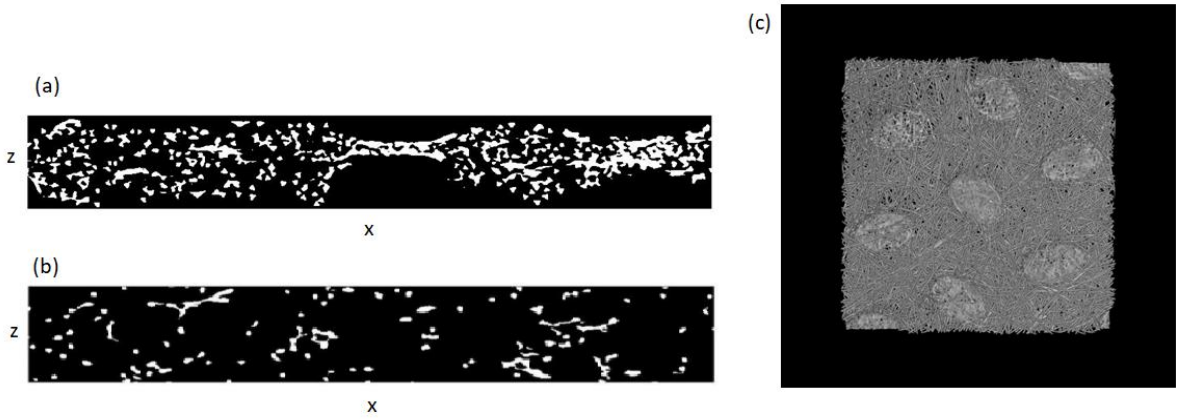

Figure 1. (a): Cross section of the P-86 layer with bonding patterns. (b): Cross section of a layer without bonding patterns. (c): top view of the P-86 layer with bonding patterns. (Tavangarrad, 2019)

The liquid phase solution used in the experiment consisted of 0.9 % by weight NaCl and distilled water solution. This liquid had a density of 1.005 g/cm^3, a viscosity of 1.019 mPa.s, and a surface tension of 72.2 mN/m.

Table 1. Properties of hydrophilic nonwoven fibrous layers used in this study.

Material	*Porosity [-]*	*Permeability [m^2]*	*Thickness [mm] at 0.3 kPa*	*Basis weight [gsm]*	*#Code*	*Surface affected by bonding process*
Polypropylene	0.84	8.3 e-11	0.170	25	PP-25	Yes
Polypropylene	0.88	2.9 e-11	0.136	10	PP-10	Yes
Polyester	0.93	1.5 e-9	0.956	60	P-60	No
Polyester	0.83	1.2 e-10	0.565	86	P-86	Yes
Cellulose	0.9	9.0 e -11	1.280	155	C-155	No
Glass fiber	0.95	9.1 e-12	1.098	120	G-120	No

2.1.2 Autoporosimeter setup

The Pore Volume Distribution Autoporosimeter (PVD-Autoporosimeter) setup, developed by Miller & Tyomkin (1994), shown in Fig. 2, was used to execute both the quasi-static and dynamic inflow/outflow experiments. The setup consisted of a sample chamber and a solution reservoir. The sample chamber contained a glass frit topped by the membrane. On top of the membrane a 50 mm diameter fibrous sample was positioned. A weight was placed on top of the sample to apply a 0.3 psi overburden pressure. The sample chamber was connected to an automatic system that controlled the overhead air pressure and temperature in the chamber.

A tube at the bottom of the sample chamber was connected to the reservoir chamber. The initial water level in the reservoir was at the same height as the top of the membrane in the sample chamber. Evaporation in the reservoir was minimized by a lid, such that the reservoir was still subjected to atmospheric air pressure. The solution reservoir was placed on a high precision balance. The mass loss or gain of the solution reservoir related to the change in saturation in the sample.

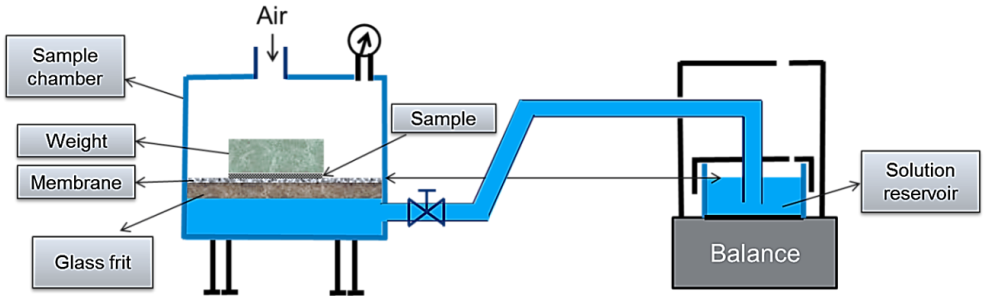

Figure 2. Schematic setup of the PVD-Autoporosimeter setup used for the experiments in this study. (Tavangarrad, 2019)

2.1.3 One-step and multistep inflow/outflow experimental setup

The PVD-Autoporosimeter was originally designed for multistep inflow and outflow experiments. In such experiments air pressure is increased or decreased in small increments. After each increment, the air pressure was kept constant until capillary fluid flow had ceased, meaning that equilibrium was reached. Next, saturation data points were measured and linked to a given capillary pressure, under the assumption that the water pressure at the top of the membrane was approximately equal to atmospheric pressure. Due to the applied 0.3 psi overburden pressure, air could only enter the sample at its sides. The time it took before equilibrium was reached was in the order of a couple of minutes. It took up to a few hours in order to measure the full quasi-static imbibition and drainage $P_c(S)$ curves for one layer.

By performing dynamic inflow and outflow experiments, transient unsaturated fluid flow conditions were evaluated. These kind of dynamic experiments required the application of one large and continuous air pressure change step, during which flow conditions did not reach equilibrium state. The large change in pressure during this experiment was fast, but not instant. Hence, the autoporosimeter software could be used to measure the change in air pressure in the overhead space of the sample chamber over time. Because the water pressure in the sample did not remain equal to the atmospheric pressure during this dynamic experiment, capillary pressure could not be derived solely from the applied air pressure. The obtained data for both the quasi-static and dynamic experiments can be used to examine the possibilities for predicting the dynamic saturation processes using statically measured hydraulic properties.

2.2 Modelling approaches

The COMSOL Multiphysics® program was used to perform the modelling. This program allows coupled systems of partial differential equations (PDEs) to be solved, using the finite element method.

A total of three different types of models have been explored. Two of these models are commonly used in research on granular soils, namely the Darcy-based two-phase flow model and the Richards equation-based model. Also the reduced continua model (RCM), which has been specifically developed to simulate the water transport between a stack of thin fibrous layers (Qin & Hassanizadeh, 2015), was used.

A total of eight individual models were constructed. A brief description of all eight models is tabulated in Table 2. It should be noted that the RCM models can be based on either single-phase flow equations, which only include the water phase as variable, or on two-phase flow equations, which include both the water and air phase as variables. For convenience, this paper will refer to the models by their model code given in Table 2. As first stage of the modelling study, data of the P-86 layer was used to examine which of these eight models is most suitable to model the conducted experiments.

Table 2. Models used in this study.

Model code	*Model Description*
1D-R	1D Richards equation-based continuum-scale model
1D-TPD	1D two-phase flow Darcy-based continuum-scale model
2D-R	2D axisymmetric Richards equation-based continuum-scale model
2D-TPD	2D axisymmetric two-phase flow Darcy-based continuum-scale model
1D-RCM(SP)	1D single-phase flow RCM
1D-RCM(TP)	1D two-phase flow RCM
2D-RCM(SP)	2D single-phase flow RCM
2D-RCM(TP)	2D two-phase flow RCM

2.2.1 Governing equations and numerical simulations

2.2.1.1 Two-phase flow Darcy-based model governing equations

Application of the mass conservation principle to a Darcy scale representative elementary volume yields the governing equation for two-phase flow in a porous medium. This mass conservation principle means that the change in the total mass of fluid phase within this REV must be balanced by the total mass flux over the REV boundary. This can be written as the following differential equation:

$$\frac{\partial}{\partial t}(\varphi \rho^{\beta} S^{\beta}) + \nabla \cdot \left(\rho^{\beta} v^{\beta}\right) = 0 \tag{1}$$

Where $\rho^{\beta}$is the mass density of fluid phase β, φ is the porosity, S^{β} is the saturation of fluid phase β, and v^{β} is the velocity of the fluid phase relative to the solid phase. When neglecting the gravity effect, which is possible due to the small vertical dimension of computational domain, v^{β} is given by the Darcy's law:

$$v^{\beta} = -\frac{K k_r^{\beta}}{\mu^{\beta}} \nabla P^{\beta} \tag{2}$$

Where K is the intrinsic permeability, k_r^{β} is the relative permeability of phase β, μ^{β} is the dynamic viscosity of phase β, and ∇P^{β} is the pressure gradient of phase β. For a scenario where water and air are the two considered fluid phases, the following system of two coupled partial differential equations is obtained:

$$\frac{\partial}{\partial t}(\varphi \rho^{w} S^{w}) - \nabla \cdot \left(\rho^{w} \frac{K k_r^{w}}{\mu^{w}} \nabla P^{w}\right) = 0 \tag{3}$$

$$\frac{\partial}{\partial t}(\varphi \rho^{a} S^{a}) - \nabla \cdot \left(\rho^{a} \frac{K k_r^{a}}{\mu^{a}} \nabla P^{a}\right) = 0 \tag{4}$$

If the compressibility of both fluids and the porous medium is neglected, the governing equations can be rewritten as:

$$\varphi \frac{\partial S^{w}}{\partial t} - \nabla \cdot \left(\frac{K k_r^{w}}{\mu^{w}} \nabla P^{w}\right) = 0 \tag{5}$$

$$\varphi \frac{\partial S^{a}}{\partial t} - \nabla \cdot \left(\frac{K k_r^{a}}{\mu^{a}} \nabla P^{a}\right) = 0 \tag{6}$$

Air and water saturation can be related with the following equation:

$$S^w + S^a = 1 \tag{7}$$

The macroscopic capillary pressure is commonly used to couple the water and air pressures in the following way:

$$P^a - P^w = P^c \tag{8}$$

Where P^a is the air pressure, P^w is the water pressure, and P^c is the capillary pressure. In this traditional approach the capillary pressure is assumed to be solely a function of saturation. However, it has been indicated that capillary pressure-saturation relationships depend on the flow dynamics (Beliav & Hassanizadeh, 2001; Hassanizadeh & Gray, 1990, 1993; Hassanizadeh et al., 1997; Mirzaei & Das, 2007). Hassanizadeh & Gray (1993) proposed a linear approximation for the change in fluid pressures under dynamic conditions, where the dynamic capillary pressure is a function of P^a, P^w, and the time derivative of the water phase saturation:

$$P^a - P^w = P^c(S^w) - \tau \frac{\partial S^w}{\partial t} \tag{9}$$

Where τ is an experimentally determined material coefficient. Based on experiments on granular soils it appeared that soil properties such as grain size distribution, porosity, and permeability, as well as fluid properties, determine the importance of dynamic effect and therefore the value of the τ. Stauffer (1978) suggested the following empirical relationship:

$$\tau = \frac{\alpha_{(B\&C)} \varepsilon \mu}{k \lambda_{(B\&C)}} \left(\frac{p^e{}_{(B\&C)}}{\rho g}\right) \tag{10}$$

Where $\alpha_{(B\&C)}$ is assumed to be constant and equal to 0.1, ε is porosity, μ is viscosity, $p^e{}_{(B\&C)}$ and $\lambda_{(B\&C)}$ are coefficients in the Brook and Corey (1964) formula for the Pc(S) relation, and k is the saturated permeability coefficient.

A well-known nonlinear relation, introduced by Van Genuchten (1980), describes the capillary pressure as a function of saturation:

$$P^c(S_e^w) = \frac{1}{\alpha}(S_e^{w\,-1/m} - 1)^{1/n} \tag{11}$$

Where α and n are fitting parameters, and with $m = 1 - 1/n$. The α parameter, sometimes replaced by its inverse $P^g = 1/\alpha$, is related to the average pore size. The value of P^g approximately corresponds to the infliction point of the P_c(S) curve. The parameters n and m are fitting parameters that are related to the pore size distribution. The effective water saturation, S_e^w, is defined as:

$$S_e^w = (S^w - S_r^w)/((1 - S_r^a) - S_r^w) \tag{12}$$

Where S_r^w is the residual water saturation and S_r^a is the residual air saturation.

The following formulas by Van Genuchten (1980) are used to describe the water and air relative permeabilities as a function of saturation:

$$k_r^w = S_e^{w\,L}\left(1 - \left(1 - S_e^{w\frac{1}{m}}\right)^m\right)^2 \tag{13}$$

$$k_r^a = (1 - S_e^w)^k \left(1 - S_e^{w\frac{1}{m}}\right)^{2m} \tag{14}$$

Where $L = 0.5$ and $k = 1/3$.

2.2.1.2 1D-TPD model domain, boundary conditions and initial conditions

For this model, only the z-dimension of the experimental setup is considered, as illustrated in Fig. 3. The domain consists of two different materials: the fabric layer and the membrane layer. The system of general equations, as described in the previous section, applies to the fabric layer. The water pressure in the fabric layer is indicated with P_f^w. The water pressure in the membrane layer is indicated as P_m^w. Over the membrane layer, the following Darcy-based general equation is considered, since this layer is always fully saturated:

$$\nabla \cdot \left(-\frac{K_m}{\mu^w} \nabla P_m^w \right) = 0 \tag{15}$$

The domain consists of three boundary nodes: the top of the fabric layer, the interface between the fabric and the membrane, and the bottom of the membrane layer. The boundary condition that represents the change in overhead air pressure at the edge of the fabric sample ($P^a_{overhead}(t)$) is applied to the top node of the domain. Therefore, the model simulates a situation in which the pressure drop is applied over the top of the fabric layer instead of the side. Further boundary and initial conditions are given in Fig. 3.

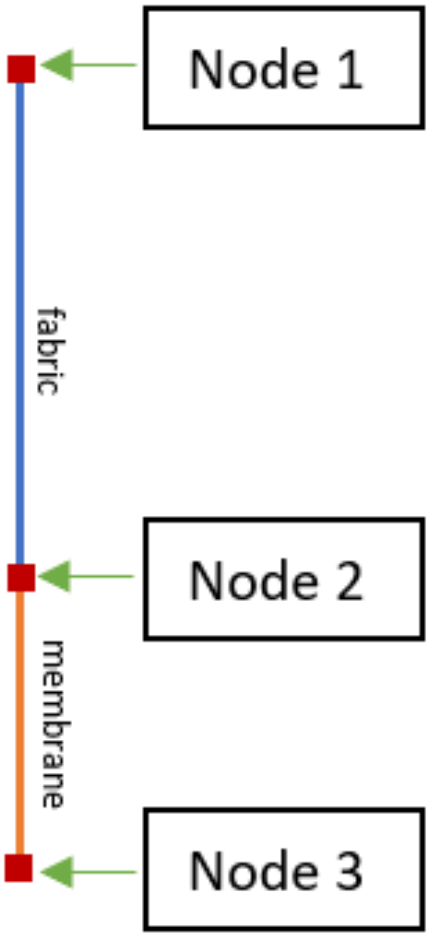

Boundary conditions

Node 1:

$$P^a = P^a_{overhead}(t)$$

$$-n \cdot \left(-\frac{K_f k_r^w}{\mu^w} \nabla P^w \right) = 0$$

Node 2:

$$P_m^w = P_f^w$$

$$n \cdot (-\frac{K_m k_r^w}{\mu^w} \nabla P_m^w) = -n \cdot (-\frac{K_f k_r^w}{\mu^w} \nabla P_f^w)$$

$$-n \cdot \left(-\frac{K_f k_r^a}{\mu^a} \nabla P^a \right) = 0$$

Node 3:

$$P^w_{m\,bottom}(t) = 0$$

Initial conditions

Fabric:

$$P^a_{init} = P^a_{overhead}(t = 0)$$

$$P^w_{f\,init} = 0$$

$$P^c_{init} = P^a_{init} - P^w_{f\,init}$$

$$S^w_{init} = (1 + (\alpha P^c_{init})^n)^{-m} = (1 + (\alpha (P^a_{init} - P^w_{f\,init})^n)^{-m}$$

$$S^a_{init} = 1 - S^w_{init}$$

Membrane:

$$P_m^w = 0$$

Figure 3. 1D-TPD model domain, boundary conditions and initial conditions.

2.2.1.3 2D-TPD model domain, boundary conditions and initial conditions

In the 2D-TPD, a two dimensional axisymmetric domain is used instead of a three dimensional domain, to reduce the computational efforts. A schematic representation of the model domain, which is a vertical cross section of the experimental setup, is given in Fig. 4. Since a weight is placed on the top of the fabric, a no flux boundary condition is specified for the top of the fabric domain (Boundary 1). The air phase can only flow through the edges of the fabric domain (Boundary 2).

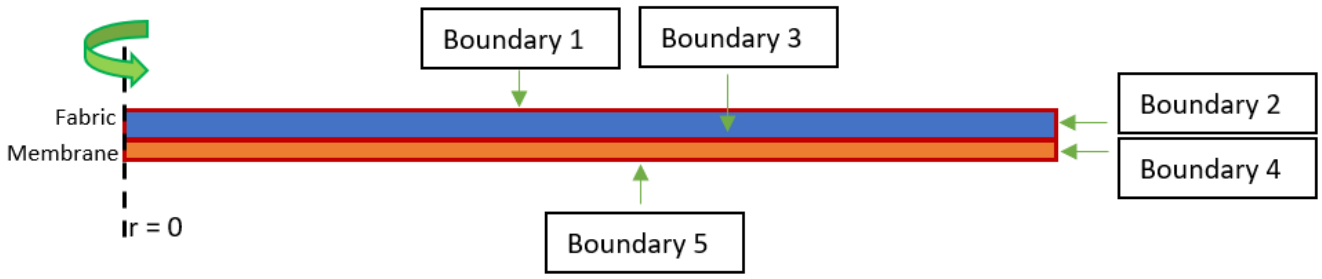

Boundary conditions

Boundary 1:

$$-n\cdot\left(-\frac{K_f k_r^w}{\mu^w}\nabla P^w\right)=0$$

$$-n\cdot\left(-\frac{K_f k_r^a}{\mu^a}\nabla P^a\right)=0$$

Boundary 2:

$$-n\cdot\left(-\frac{K_f k_r^w}{\mu^w}\nabla P^w\right)=0$$

$$P^a = P^a_{overhead}(t)$$

Boundary 3:

$$P_m^w = P_f^w$$

$$n\cdot\left(-\frac{K_m k_r^w}{\mu^w}\nabla P_m^w\right) = -n\cdot\left(-\frac{K_f k_r^w}{\mu^w}\nabla P_f^w\right)$$

$$-n\cdot\left(-\frac{K_f k_r^a}{\mu^a}\nabla P^a\right)=0$$

Boundary 4:

$$-n\cdot\left(-\frac{K_f}{\mu^w}\nabla P_m^w\right)=0$$

Boundary 5:

$$P^w_{m\,bottom}(t)=0$$

Initial conditions

Fabric:

$$P^a_{init} = P^a_{overhead}(t=0)$$

$$P^w_{f\,init}=0$$

$$P^c_{init} = P^a_{init} - P^w_{f\,init}$$

$$S^w_{init} = (1+(\alpha P^c_{init})^n)^{-m} = (1+(\alpha(P^a_{init}-P^w_{f\,init})^n)^{-m}$$

$$S^a_{init} = 1 - S^w_{init}$$

Membrane:

$$P_m^w = 0$$

Figure 4. 2D-TPD model domain, boundary conditions and initial conditions.

2.2.1.4 *Richards equation-based model governing equations*

When the transport of only water and air in the unsaturated zone and under certain specific conditions are considered, the two-phase flow model can be simplified to a model based on the Richards equation. At a temperature of 20 °C, the air viscosity is about 55 times smaller than the water viscosity (Szymkiewicz, 2013). This implies that the air mobility is by approximately the same factor higher than the water mobility, if the relative permeabilities of both phases are equal. Any occurring air pressure difference in space will therefore equilibrate much faster than any water pressure difference in space. Also, it can often be assumed that the air phase is continuous in the pore space and that it is in contact with the atmosphere. If one neglects the variations of the atmospheric pressure, and assumes the air phase to be infinitely mobile, the pore air can be considered as a constant through time and space, and equal to the atmospheric pressure. If all specific conditions are met, the equation for air flow (Eq. 6) can be eliminated from the system of governing equations. When the reference atmospheric pressure is assumed to be 0, Eq. (8) and Eq. (9) can respectively be rewritten as:

$$-P^w = P^c \tag{16}$$

$$-P^w = P^c(S^w) - \tau \frac{\partial S^w}{\partial t} \tag{17}$$

2.2.1.5 *1D-R model domain, boundary conditions and initial conditions*

The model domain used for the 1D-R model (Fig. 5) is the same as that for the 1D-TPD model (Fig. 3.). Because a variation in air pressure is applied in the experiment, air pressure is not a constant. It is therefore not possible to simply eliminate the air phase PDE from the model. In order to be able to use the Richards model anyway, an increasing water pressure boundary condition at the bottom of the membrane (Node 3) is implemented to simulate the effect of a decreasing air pressure at the sides (Node 1). After application of this 'trick', it is possible to assume the air pressure to be constant, and the PDE for air flow (Eq. 6) can be eliminated from the system of governing equations.

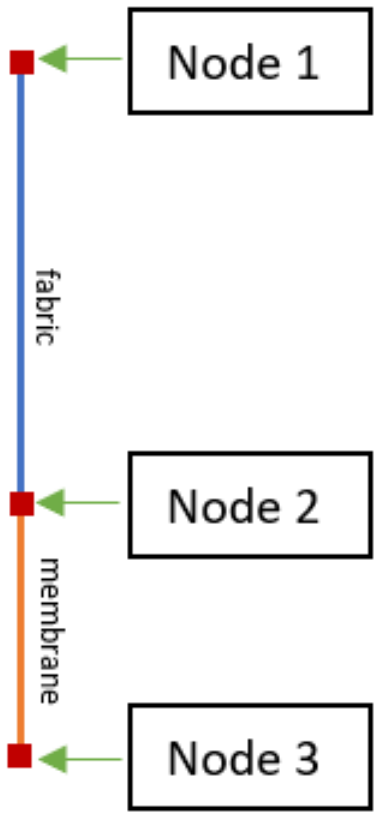

Boundary conditions

Node 1:

$$-n \cdot \left(-\frac{K_f k_r^w}{\mu^w} \nabla P^w\right) = 0$$

Node 2:

$$P_m^w = P_f^w$$

$$n \cdot \left(-\frac{K_m k_r^w}{\mu^w} \nabla P_m^w\right) = -n \cdot \left(-\frac{K_f k_r^w}{\mu^w} \nabla P_f^w\right)$$

Node 3:

$$P^w_{m\ bottom}(t) = -P^a_{overhead}(t)$$

Initial conditions

Fabric:

$$P^a_{init} = P^a_{overhead}(t=0)$$

$$P^w_{f\ init} = -P^a_{overhead}(t=0)$$

$$P^c_{init} = -P^w_{f\ init}$$

$$S^w_{init} = (1 + (\alpha P^c_{init})^n)^{-m} = (1 + (\alpha(-P^w_{f\ init})^n)^{-m}$$

$$S^a_{init} = 1 - S^w_{init}$$

Membrane:

$$P_m^w = -P^a_{overhead}(t=0)$$

Figure 5. 1D-R model domain, boundary conditions and initial conditions.

2.2.1.6 2D-R model domain, boundary conditions and initial conditions

The model domain used for the 2D-R model (Fig. 4) is the same as that for the 2D-TPD model (Fig. 6). Again, an increasing water pressure boundary condition at the bottom of the membrane (Boundary 5) was implemented to simulate the effect of a decreasing air pressure at the sides (Boundary 2).

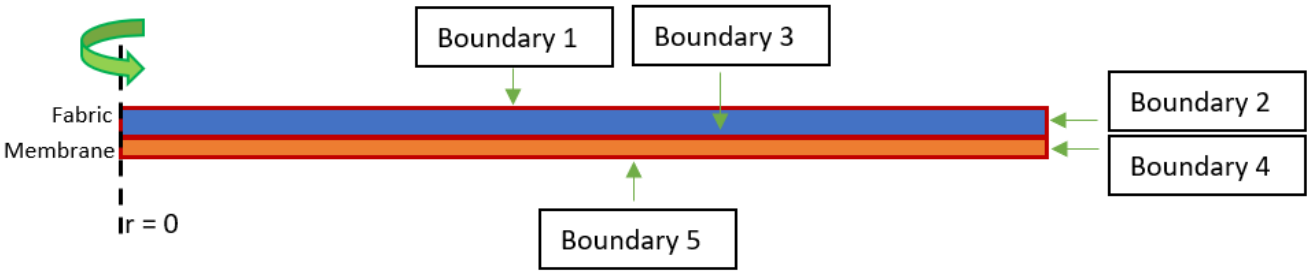

Boundary conditions

Boundary 1 & 2:

$$-n \cdot \left(-\frac{K_f k_r^w}{\mu^w} \nabla P^w\right) = 0$$

Boundary 3:

$$P_m^w = P_f^w$$

$$n \cdot \left(-\frac{K_m k_r^w}{\mu^w} \nabla P_m^w\right) = -n \cdot \left(-\frac{K_f k_r^w}{\mu^w} \nabla P_f^w\right)$$

Boundary 4:

$$-n \cdot \left(-\frac{K_f}{\mu^w} \nabla P_m^w\right) = 0$$

Boundary 5:

$$P_{m\,bottom}^w(t) = -P_{overhead}^a(t)$$

Initial conditions

Fabric:

$$P_{init}^a = P_{overhead}^a(t=0)$$

$$P_{f\,init}^w = -P_{overhead}^a(t=0)$$

$$P_{init}^c = -P_{f\,init}^w$$

$$S_{init}^w = (1 + (\alpha P_{init}^c)^n)^{-m} = (1 + (\alpha(-P_{f\,init}^w)^n)^{-m}$$

$$S_{init}^a = 1 - S_{init}^w$$

Membrane:

$$P_m^w = -P_{overhead}^a(t=0)$$

Figure 6. 2D-R model domain, boundary conditions and initial conditions.

2.2.1.7 RCM(TP) governing equations

In the reduced continua model, the vertical dimension of the original continuum-scale modelling domain is reduced to a horizontal line. The main reason for this reduction of dimensionality is because the representative elementary volume may not be defined for a thin porous media. This is due to the fact that only a few pores exist along the thickness. Therefore, Qin and Hassanizadeh (2015) developed a model in which the equations of vertical water flow and the in-layer macroscale balance laws, are formulated in terms of thickness-averaged material properties. Interaction between the membrane and the fabric are accounted for by exchange terms for mass and momentum.

The RCM can be based on either two-phase flow equations or single-phase flow equations. In the RCM(TP) approach, the mass conservation equations of water and air in layer i are given as:

$$\left.\frac{\partial(b\rho^w\varphi S^w)}{\partial t}\right|_i - \boldsymbol{\nabla}_h \cdot \left(b\rho^w \frac{k_r^w K}{\mu^w}\, \boldsymbol{\nabla}_h P^w\right)\Big|_i = Q_T^w|_i + Q_B^w|_i \tag{18}$$

$$\left.\frac{\partial(b\rho^a\varphi S^a)}{\partial t}\right|_i - \boldsymbol{\nabla}_h \cdot \left(b\rho^a \frac{k_r^a K}{\mu^a}\, \boldsymbol{\nabla}_h P^a\right)\Big|_i = Q_T^a|_i + Q_B^a|_i \tag{19}$$

Where $Q_{\mathrm{T}}^{\mathrm{w}}|_i$ and $Q_{\mathrm{B}}^{\mathrm{w}}|_i$ denote the top and bottom fluxes of water for layer *i*, $Q_T^a|_i$ and $Q_B^a|_i$ indicate air flux from the top and bottom of layer *i*, and b is the material thickness. In the case of a system consisting of a sample layer on top of the fully saturated membrane, the total of four governing equations reduce to three, and are expressed in the following form:

$$\left.\frac{\partial(b\rho^w\varphi S^w)}{\partial t}\right|_f - \boldsymbol{\nabla}_h \cdot \left(b\rho^w \frac{k_r^w K}{\mu^w}\, \boldsymbol{\nabla}_h P^w\right)\Big|_f = Q_S^w|_f + Q_B^w|_f \tag{20}$$

$$\left.\frac{\partial(b\rho^a\varphi S^a)}{\partial t}\right|_f - \boldsymbol{\nabla}_h \cdot \left(b\rho^a \frac{k_r^a K}{\mu^a}\, \boldsymbol{\nabla}_h P^a\right)\Big|_f = Q_S^a|_f + Q_B^a|_f \tag{21}$$

$$-\boldsymbol{\nabla}_h \cdot \left(b\rho^w \frac{k_r^w K}{\mu^w}\, \boldsymbol{\nabla}_h P^w\right)\Big|_m = Q_T^w|_m + Q_B^w|_m \tag{22}$$

Where the subscripts f and m refer to the fabric sample and the membrane respectively. It should be noted that since the top of the fabric is concealed, the mass fluxes apply to the sides of the fabric and not to the top. The S subscript is therefore used to define the mass fluxes $Q_S^w|_f$ and $Q_S^w|_f$ at the side of the fabric.

One difficulty, concerning the way of modelling the dynamic water exchange at the layer interface, has been addressed by Qin and Hassanizadeh (2014, 2015). Based on thermodynamic considerations and the simplifying assumption of slow flow through the porous layers, which allows for the neglection of the effect of kinetic energy, Qin & Hassanizadeh (2014) proposed the following equation, relating the inter layer fluxes to their pressure difference:

$$Q_B^w|_f = -Q_T^w|_m = \Pi_m\left(P_f^w - P_m^w\right) \tag{23}$$

Where Π_m is the mass transfer coefficient. This parameter is specific to the material properties of the two layers, but it also considers the nature of the contact between the two layers. After assuming continuity of the flow rate through the contact plane, Qin and Hassanizadeh (2015) proposed the following equation for the mass transfer coefficient:

$$\Pi_m = \frac{2}{b_f + b_m}\rho^w \frac{\overline{K_t}}{\mu^w} f(S_f^w, S_m^w) \tag{24}$$

$$\overline{K_t} = \frac{b_f + b_m}{b_m K_f + b_f K_m} K_f K_m \tag{25}$$

Where K_t is the effective intrinsic through-plane permeability of the two layers, and $f(S_f^w, S_m^w)$ is a general saturation function used to represent the relative permeability for liquid water transport through the interface. Qin & Hassanizadeh (2015) proposed the following equation for the saturation function:

$$f(S_f^w, S_m^w) = \frac{1}{2}((S_m^w)^{y1} + (S_f^w)^{y2}) \tag{26}$$

Where $y1$ and $y2$ are fitting parameters. Since the membrane is always saturated, this equation has a minimum value of 0.5. It was desired to also obtain a saturation function with a range between zero and one. Multiple variations to this original saturation function have been examined in order to get a grasp of the main processes at hand. Besides Eq. (26), three other types of saturation functions are documented in this study:

$$f(S_f^w) = S_f^{wy} \tag{27}$$

$$f(S_f^w, S_m^w) = A\frac{S_f^{wx} + S_m^{wx}}{2} + B\frac{2(S_f^{wx} S_m^{wx})}{(S_f^{wx} + S_m^{wx})} \tag{28}$$

$$f(S_f^w, S_m^w) = \begin{cases} Z & S_f^w < q \\ \dfrac{S_f^{w3} + S_m^{w3}}{2} & S_f^w > q \end{cases} \tag{29}$$

Where y, x, A, B, and Z are fitting parameters. Eq. (27) is a simple power function of the water saturation. Eq. (28) is a combination of the arithmetic mean ($A\frac{S_f^{wx}+S_m^{wx}}{2}$) and the harmonic mean ($B\frac{2(S_f^{wx} S_m^{wx})}{(S_f^{wx}+S_m^{wx})}$) of the saturations of the two considered layers. The sum of A and B is 1. The saturation function of Eq. (29) was included because it is independent of initial saturation, which makes physical sense since no connecting water pathways are present within the fabric at the initial low water saturation stage of the experiment. The parameter q here represents a saturation threshold value after which interconnecting water pathways start to form.

Based on preliminary results of these RCM approaches, where the saturation functions of Eqs. (26 to 29) are used, a second mass transfer coefficient is developed. Two effects are taken into account within this new mass transfer coefficient. First, water saturation must build in one of the layers and the interlayer pore space in order to have a fluid connection between the two layers. Since the membrane is always fully saturated in this study, the saturation build up in the interlayer pore space has to be considered only. Second, the flux between the layers depends on the water transfer rate in the connected pores of interlayer space, and therefore on the quality of the contact between the two layers. As an example, for a system of two layers with a very large gap in between, the saturation threshold build up in one of the layers is approximately 1 and the contact dependent transfer rate coefficient is about zero, so no fluid flow from one to the other layer will take place. By decreasing the gap and making more contacts, the saturation threshold reduces, and the transfer rate increases. In this study, the membrane is fully saturated and an overburden pressure is applied, so the water saturation threshold is already passed. However, the interface transfer rate, which is incorporated in the model through an interface contact quality coefficient (λ), has a major role in the exchange of water between the membrane and the fibrous layer. The new mass transfer coefficient can be given in the following form:

$$\Pi_m = \begin{cases} \lambda\, C & S_f^w < S_r^w{}_f \\ \dfrac{2}{b_m + b_f}\rho^w \dfrac{\overline{K_t}}{\mu^w}\,\lambda & S_f^w > S_r^w{}_f \end{cases} \tag{30}$$

$$\overline{K_{\mathrm{t}}} = \frac{b_m + b_f}{b_f K_m + b_m K_f k_f^{\mathrm{r}}} K_m K_f k_f^{\mathrm{r}} \tag{31}$$

Where $S_r^w{}_f$ is the residual saturation of the fibrous layer, and C is a constant coefficient which is assumed to be the same for all fabric samples. The assumption here is that before water saturation in the sample reaches the residual saturation, connected pathways are not created in the sample, and the mass transfer coefficient only depends on the interface properties. The mass transfer coefficient is therefore independent of saturation below the residual water saturation. After reaching $S_r^w{}_f$, the harmonic mean of relative permeability determines the exchange between the two layers. The Van Genuchten (1980) based relative permeability parameters are implemented in the effective intrinsic permeability term of the two layers, as was done by Tavangarrad et al. (2018).

Since water cannot leave the fabric, the water flux at the sides of the fabric is zero:

$$Q_S^w|_f = 0 \tag{32}$$

The air flux at the bottom of the fabric is also zero, because the membrane is always fully saturated:

$$Q_B^a|_f = 0 \tag{33}$$

The equation for $Q_S^a|_f$ is a function of the difference in average air pressure in the fabric and the applied overhead pressure ($P_{overhead}^a(t)$):

$$Q_S^a|_f = -\rho^a \frac{K_m k_r^a}{\mu^a} \frac{P^a - P_{overhead}^a(t)}{b_f/d} \tag{34}$$

Where coefficient d is a geometric constant related to the location of average pressure in the fabric layer. The flux at the bottom of the membrane is given as:

$$Q_B^w|_m = -\rho^w \frac{K_m}{\mu^w} \frac{P_m^w - P_{m\,bottom}^w(t)}{b_m/d} \tag{35}$$

Eqs. (7 to 14) are valid for defining hydraulic properties in the RCM model.

2.2.1.8 1D-RCM(TP) and 2D-RCM(TP) model domains, boundary conditions and initial conditions

In the 1D-RCM(TP) model, the round membrane and fabric layers are represented as two one-dimensional lines (Fig. 7). The 2D-RCM(TP) domain is represented as two circles on top of each other (Fig. 8). The initial conditions are equal to the initial conditions used for the continuum-scale two-phase flow models. No specific boundary conditions are defined in the reduced continuum models since the boundary fluxes are already implicit in the governing equations. One exception is the 2D-RCM(TP) model where the COMSOL Multiphysics® model was constructed such that the $Q_S^a|_f$ flux was applied to the side boundary of the model domain only (see Fig. 8). Note that in the 1D-RCM(TP) model the $Q_S^a|_f$ flux is applied to the top of the domain and not to the side (Fig. 7), as was the case for the 1D-TPD model.

Figure 7. Schematic representation of 1D-RCM(TP) model domain.

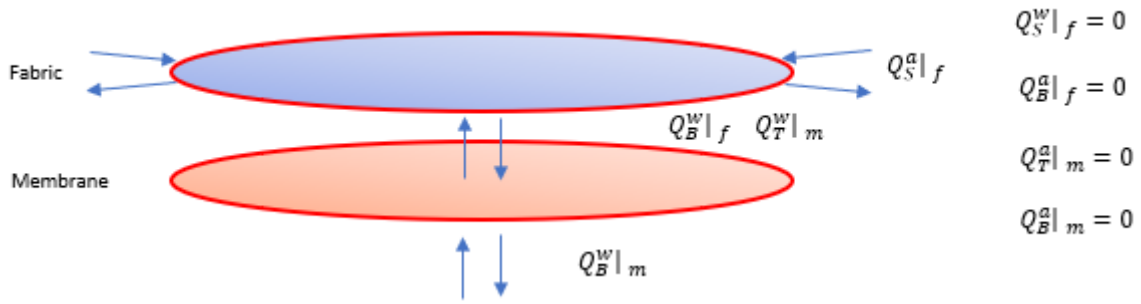

Figure 8. Schematic representation of 2D-RCM(TP) model domain.

2.2.1.9 RCM(SP) governing equations

Consistent with the Richards assumption, we consider the water phase only. The air phase is assumed to be constant at atmospheric air pressure and infinitely mobile. The governing equations then become:

$$\left.\frac{\partial(b\rho^w\varphi S^w)}{\partial t}\right|_f - \boldsymbol{\nabla}_h \cdot \left(b\rho^w \frac{k_r^w K}{\mu^w}\, \boldsymbol{\nabla}_h P^w\right)\Big|_f = Q_T^w|_f + Q_B^w|_f \tag{36}$$

$$-\boldsymbol{\nabla}_h \cdot \left(b\rho^w \frac{k_r^w K}{\mu^w}\, \boldsymbol{\nabla}_h P^w\right)\Big|_m = Q_T^w|_m + Q_B^w|_m \tag{37}$$

The same 'trick' as in the continuum-scale Richards models was applied, where an increasing water pressure boundary condition at the bottom of the membrane was used to simulate the effect of a decreasing air pressure at the sides of the fabric ($P^w_{m\,bottom}(t) = -P^a_{overhead}(t)$). The water flux at the bottom of the membrane is now defined as:

$$Q_B^w|_m = -\rho^w \frac{K_m}{\mu^w} \frac{P_m^w - (-P^a_{overhead}(t))}{b_f/d} \tag{38}$$

In combination with Eqs. (7 to 14) the RCM governing equations can be solved to compute the average saturation (S_f^w) through time.

2.2.1.10 1D-RCM(SP) and 2D-RCM(SP) model domains, boundary conditions and initial conditions

The model domains for the RCM(SP) models are the same as for the RCM(TP) models (Figs. 9 and 10). Note that al mass fluxes for air are eliminated. The initial conditions are equal to the initial conditions in the continuum-scale Richards models.

Figure 9. Schematic representation of 1D-RCM(SP) model domain.

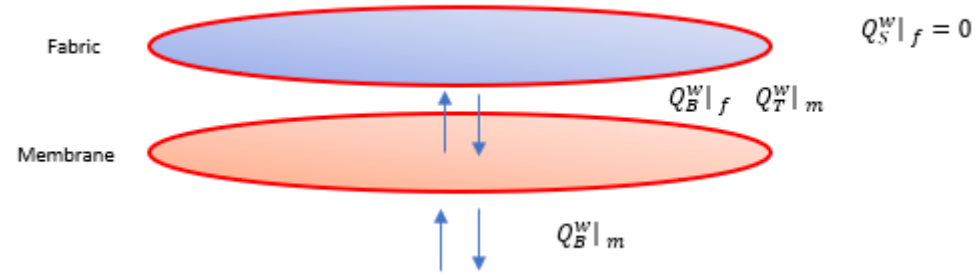

Figure 10. Schematic representation of 2D-RCM(SP) model domain.

3 Results and Discussion

3.1 Quasi-static experiment results

The experimental Pc(S) curves for both inflow and outflow experiments, as well as the best possible Van Genuchten (VG) fit of the data, are shown in Fig. 11. The fitted VG parameters of all layers are tabulated in Table 3. The P-60 layer has the lowest capillarity and the G-120 layer shows highest capillarity among all sample layers.

Table 3. Fitted Van Genuchten (1980) parameters of the quasi-static measured Pc(S) curves, and residual water saturation.

#Code	α imbibition [1/Pa]	n imbibition [-]	α drainage [1/Pa]	n drainage [-]	S_r^w
PP-25	0.0014	5.15	0.0005	7.16	0.06
PP-10	0.00096	2.68	0.00024	3.76	0.1
P-60	0.073	4.32	0.0017	6.50	0.01
P-86	0.0012	5.06	0.00046	4.52	0.09
C-155	0.00058	3.62	0.00029	3.5	0.08
G-120	0.00022	4.98	0.000105	2.00	0.2

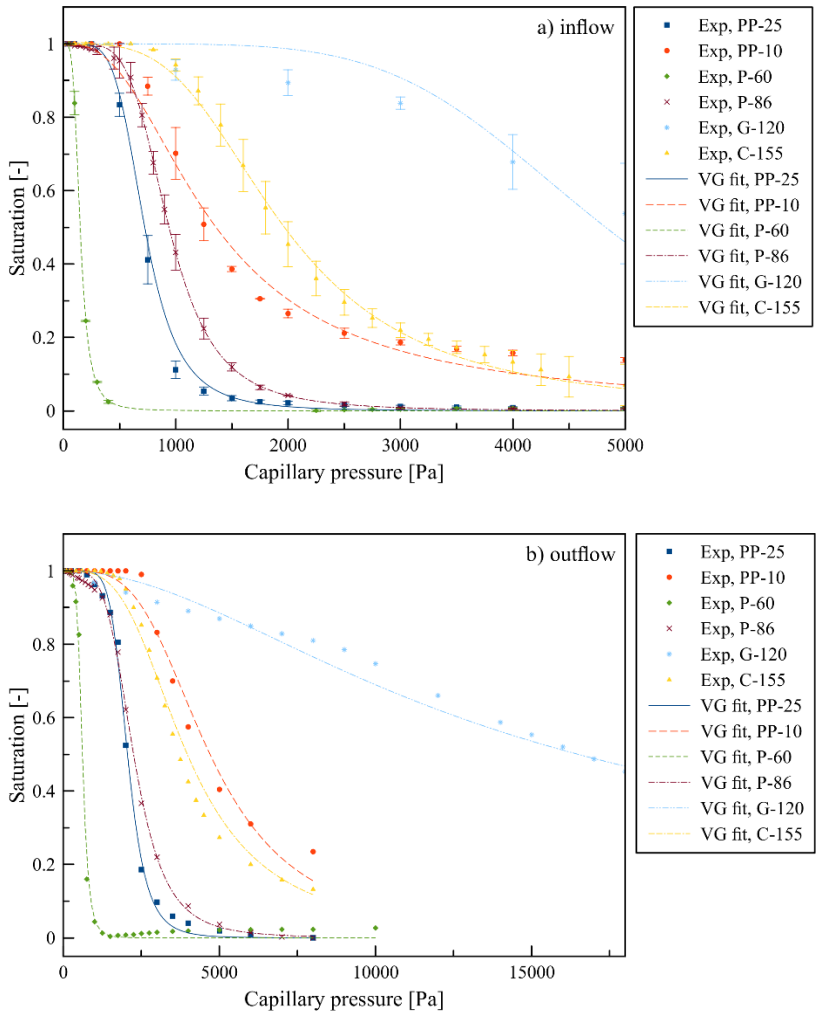

Figure 11. Measured data points and VG fitted curves of capillary pressure-saturation relationship for six nonwoven fibrous layers used in this study. Results are given for the inflow (a) and outflow (b) experiments.

3.2 Dynamic inflow experiments

Plots of air pressure variation and wetting saturation over time, for the dynamic inflow experiments, are given in Fig. 12. For the PP-10 layer, results of a replicate are included to show that differences in air pressure boundary conditions cause a slight difference in water saturation evolution. For all layers, except for the G-120 layer, the initial air pressure is 4500 Pa. After approximately 3 seconds, the air pressure inside the sample chamber is decreased and reaches to zero in less than 15 seconds. Different wetting evolutions are observed for all the layers. The C-155 layer wets fastest and becomes almost fully saturated in less than 7 seconds, while for the P-60 layer it takes more than 40 seconds to become almost fully saturated. The measured initial water saturations correspond to initial state of air pressure inside the chamber.

The capillarity of the G-120 sample is higher than that of other materials. In order to start the inflow experiment with initially low water saturation to cover a wide range of saturations, an initial air pressure of 20000 Pa is used in this experiment. For the most materials, water initially moves rapidly into the layer, after which further saturation stagnates between a saturation of 0.8 and 0.95. Most experiments show a second phase of increasing saturation until the sample reaches equilibrium in about one minute.

The exact moment of water saturation increase depends on initial water saturation values and air entry pressures. For example, the low air entry pressure of P-60 results in late water infiltration of this sample material compared to other samples.

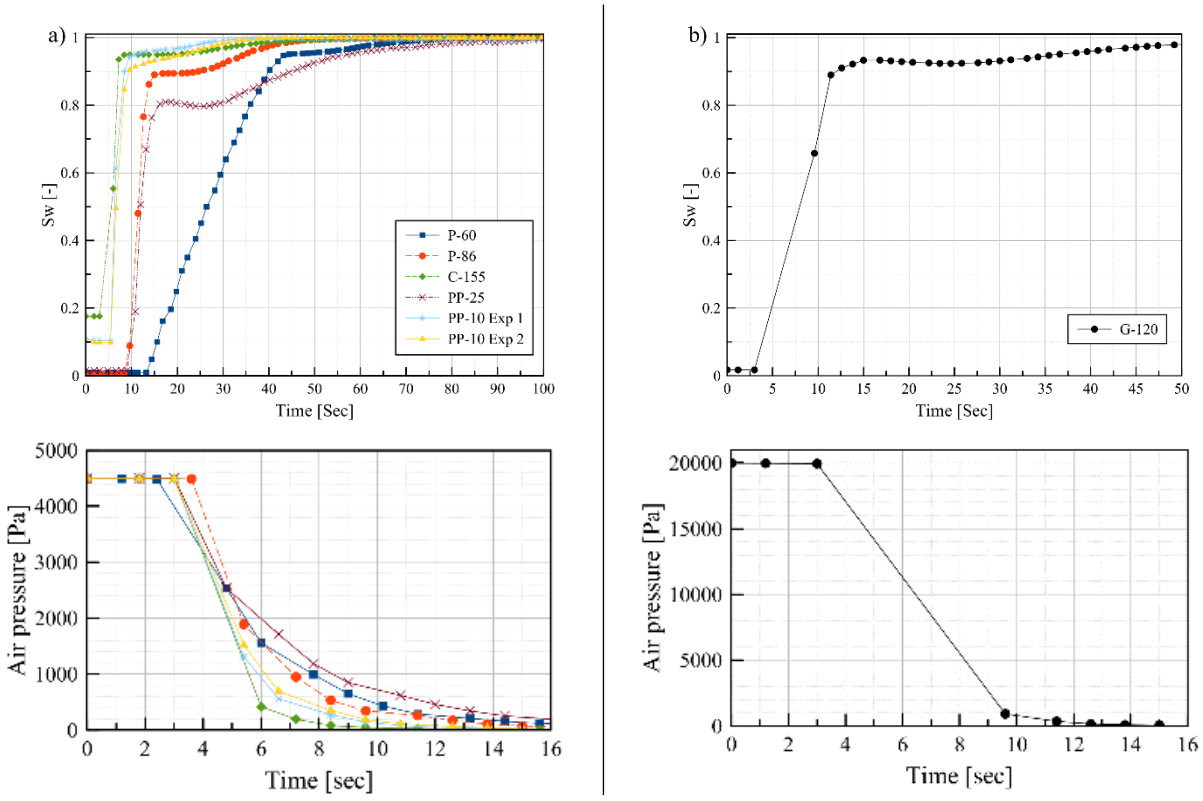

Figure 12. Water saturation evolution of all materials when air pressure drops from 4500 or 20000 Pa to zero within approximately 15 seconds. Experimental results of: layers P-60, P-86, C-155 and PP-25 (a), two replicates of layer PP-10 where a higher air pressure at the boundary result in slower change of saturation over time (a), and layer G-120 (b), are given.

3.2.1 Model evaluation stage based on P-86

The 1D-R, 1D-TPD, and 2D-R model approaches result in almost identical saturation curves (Fig. 13). Only the 2D-TPD model yields different results, because the vertical flow component plays a significant role in this model. Due to the experiment setup, with an applied weight on top, entrapment of air occurs in the center of the sample layer. As the air pressure drops at the edge of the sample (Boundary 2 in Fig. 5), S^w increases faster at this edge compared to the center of the sample. This leads to a relatively low S^a and thus low effective permeability of air at the edge, in that way trapping the air that is still in the center of the sample. This entrapment effect is observed at the upper edge of the S^w vs. time curve, since that is when air gets trapped. All four models yield similar results at the early stage (i.e. at low S^w). The number of mesh elements for each of the constructed models are included in Table 4. The 2D-TPD model is the best model to simulate the executed experiments, since it takes the effect of the horizontal flow component into account.

All models yield a S^w versus time curve where the change in overhead air pressure results in an immediate change in S^w. The experimental results of the P-86 layer on the other hand show that there is a lag between the initial drop in air pressure, and the moment when S^w in the sample starts to increase. In other words, during the air pressure driven imbibition of the sample, there is a lag between air pressure drop and the initial moment at which water from the membrane starts to enter the fabric sample.

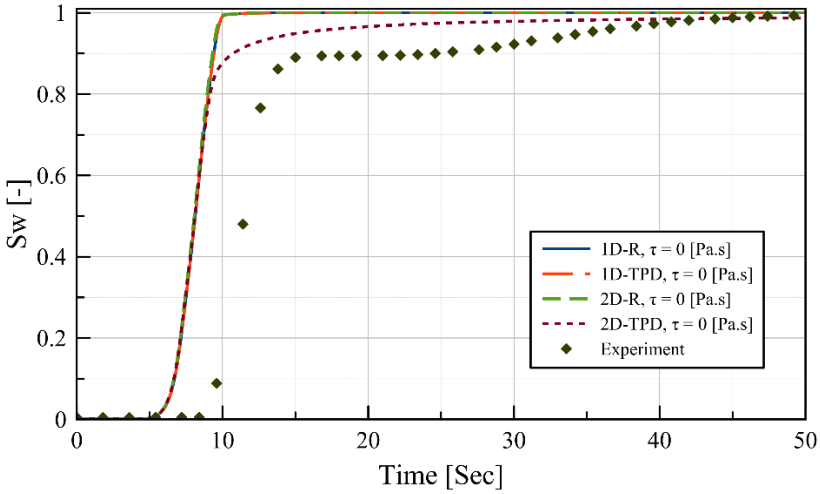

Figure 13. Comparison of simulated water saturation evolution curves during imbibition, using 4 different continuum-scale models. Dynamic capillarity effect is not included (i.e. τ = 0 Pa.s).

Table 4. Number of mesh elements used in the constructed models.

Sample layer	1D-R	1D-TPD	2D-R	2D-TPD	1D-RCM	2D-RCM
P-86	150	150	5330	44522	149	2170
PP-25	-	-	-	25212	-	2170
PP-10	-	-	-	26712	-	2170
P-60	-	-	-	15290	-	2170
C-120	-	-	-	11546	-	2170
G-155	-	-	-	22040	-	2170

Due to the fiber structure of the fabric, the horizontal permeability is larger than the vertical permeability. The effect of the implication of anisotropy in the model is illustrated in Fig. 14. For the P-86 layer this implies a vertical permeability of 7.59e-11 m^2 and a horizontal permeability of 4.78e-10 m^2. After including anisotropy in the model, the overall horizontal permeability is slightly larger, leading to less entrapment of air. Therefore the S^w versus time curve bends towards its horizontal asymptote at higher S^w.

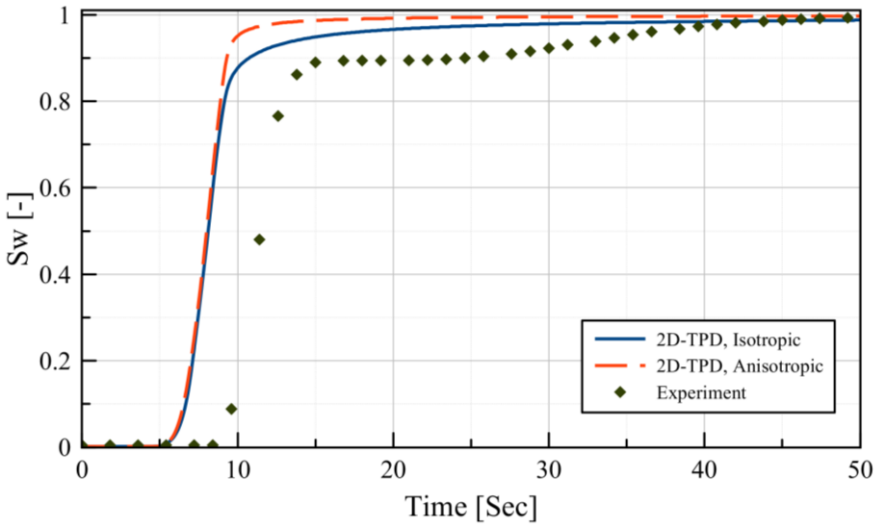

Figure 14. Indication of the effect of anisotropy for the P-86 layer. One simulation with an isotropic and one simulation with an anisotropic 2D-TPD model.

In this study, relative permeabilities are calculated by means of the VG fitting parameters (Eqs. 13 and 14). These relative permeability functions are commonly used for modelling fluid flow through granular soils. Their application in modelling research on fibrous layers has been successful, but is much less common. Therefore relative water and air permeabilities have also been examined through pore scale analysis, using the GeoDict® program. These pore scale analysis indicate that the P-86 sample has a relative water permeability (k_r^w) of zero when S^w is below a value of between 0.1 and 0.2 (Table 5 and Fig.15a). This is caused by the absence of connecting pathways. The same is true for the relative air permeability (k_r^a) when S^a is below a value of between 0.5 and 0.7 (Table 5 and Fig.15b). The difference between the two relative permeability evaluation methods is clearly illustrated in Fig. 15.

Table 5. Examined relative air and water permeabilities in the P-86 layer, using GeoDict® pore scale analysis.

S^w	0	0.053981	0.095837	0.202939	0.294538	0.503393	0.69996	1
k_r^w	0	0	0	0.000226	0.002168	0.066184	0.644609	1
S^a	0	0.30004	0.496607	0.705462	0.797061	0.904163	0.946019	1
k_r^a	0	0	0	0.097955	0.298247	0.646904	0.800789	1

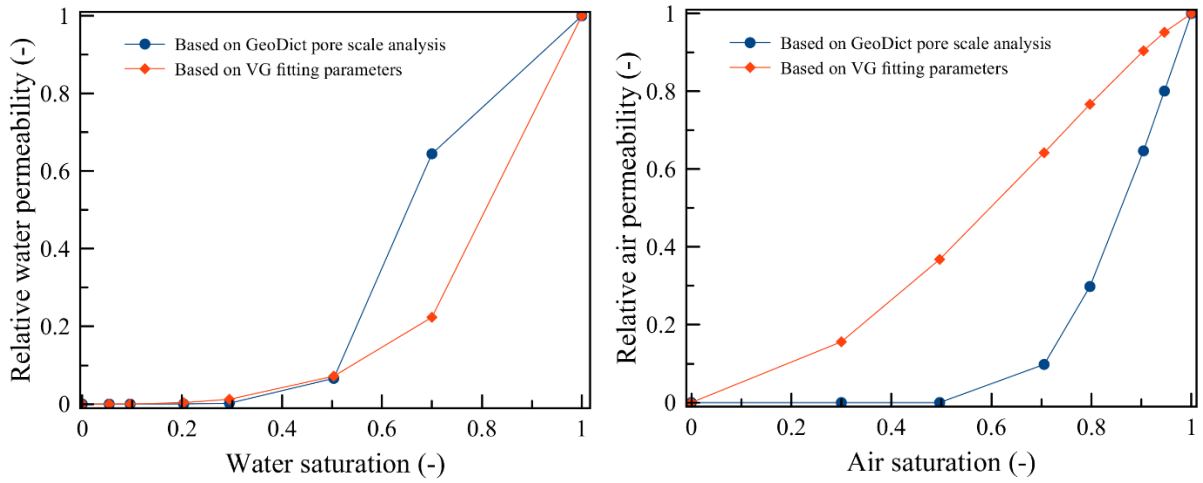

Figure 15. Relative permeabilities in the P-86 layer: (a) k_r^w based on VG parameters (Eq. 13) and k_r^w based on pore scale analysis, (b) k_r^a based on VG parameters (Eq. 14) and k_r^a based on pore scale analysis.

The effect of the relative permeability is studied by implementing the GeoDict® based relative permeabilities in the 2D-TPD model. It is not possible to include a relative permeability of zero in the model, therefore three different functions were used to replace the zero values in Table 5. These three functions are: linear functions (i.e. $k_r^w \sim S_w$ and $k_r^a \sim S_a$), the functions $k_r^w \sim {S_w}^{0.5}$ and $k_r^a \sim {S_a}^{0.5}$, and a power function with a value equal to the power regression of all non-zero k_r^a and k_r^w values in Table 5 (i.e. $k_r^w \sim {S_w}^{5.6}$ and $k_r^a \sim {S_a}^{6.7}$). Graphs of these k_r^w and k_r^a functions are given in Appendix 1.

Appendix 2 shows the results of the 2D-TPD model simulations after application of the different relative permeability curves. Fig. A2 indicates that the models in which k_r^w and k_r^a are based on the GeoDict® results, and where the zero values are replaced by relatively high values (i.e. the linear and $k_r \sim S^{0.5}$ function), yield similar results to the model simulations with VG based k_r^w and k_r^a values. The model simulation in which k_r^w and k_r^a are based on a high power relation, and where the zero values are thus replaced by relatively low values, yields a significantly different result. A slight lag between the moment of atmospheric pressure drop and the initial moment of wetting of the sample is simulated, although still not as evident as the lag observed in the experimental results (see Fig. A2).

The exact k_r^w and k_r^a functions at respectively high S_w and S_a have negligible impact on the simulation results (Fig. A2). The simulation with VG based and GeoDict® based relative permeability functions yield similar results as long as k_r^w and k_r^a are relatively high at respectively low S_w and S_a. When, conform the GeoDict® pore scale analysis results, k_r^w and k_r^a are close to zero at respectively low S_w and S_a, simulation results start to differentiate (Fig. A2). Low k_r^w up to $S_w = 0.2$ cause a lag in the entrance time of water into the sample. Low k_r^a up to $S_a = 0.7$ cause the S_w versus time curve to bend towards its horizontal asymptote value more gradually and at a lower S_w, as a consequence of enhanced air entrapment in the center of the sample.

3.2.2 Simulation of all six fibrous layers

The 2D-TPD model is used to do a sensitivity analysis on the effect of dynamic capillarity and relative water and air permeabilities at low saturation. Simulations of all six layers are performed. Variations to the τ value, to the k_r^w function below a S_w value of 0.2, and to the k_r^a function below a S_a value of 0.5, are applied. For the k_r^w and k_r^a functions below $S_w = 0.2$ and $S_a = 0.5$ respectively, a power function is used. In all simulations, relative permeability functions of Eqs. (13 and 14) are employed for the k_r^w and k_r^a functions when $S_w > 0.2$ and $S_a > 0.5$. At these 'high saturation' conditions, the relative air and water permeabilities have only minor impact on the model results. Therefore, the time consuming GeoDict® pore scale analysis are unnecessary for each individual layer.

For most layers, a total of 10 simulations have been done (Fig. 16). Three different k_r functions are applied in combination with three different τ values, resulting in a total of 9 different simulation. In the tenth simulations τ and k_r are changed to find the best correspondence with the experimental data. Below, the main results will be highlighted. The wetting curves of all simulations can be found in Appendix 3. Note that some of the simulations are missing. This is because some of the simulations are unnecessary, as the original VG based simulations yielded good results already. Also, some simulation variations yielded numerical issues, and are therefore not included.

$\tau = 0$		$k_{r\,(Sw<0.2)}^{w} = VG\ based\ \&$ $k_{r\,(Sa<0.5)}^{a} = VG\ based$
$\tau = 1000$		$k_{r\,(Sw<0.2)}^{w} = S_w{}^{9}\ \&$ $k_{r\,(Sa<0.5)}^{a} = VG\ based$
$\tau = Stauffer\ based$		$k_{r\,(Sw<0.2)}^{w} = S_w{}^{9}\ \&$ $k_{r\,(Sa<0.5)}^{a} = S_a{}^{3}$
$\tau = best\ estimate\ \&\ k_{r\,(Sw<0.2)}^{w} = best\ estimate\ \&\ k_{r\,(Sa<0.5)}^{a} = best\ estimate$		

Figure 16. Sensitivity study on dynamic capillarity and relative permeability functions using different combination of them in our study.

Results of simulations in which normal VG based relative permeabilities are considered, and where dynamic capillarity is not included, are given in Figs. 17 and 18. The common feature of modeling results for the three layers that have surficial bonding patterns (PP-10, PP-25, and P-86) is that the simulated saturation curves forge ahead of experimental data (Fig 17.). The simulation results of the other layers (P-60, C-155, G-120) do not show this discrepancy at the initial low S_w part of the curve (Fig. 18). The P-60, C-155 and G-120 simulations therefore yield a better fit with the experimental data. The P-60 layer shows a discrepancy with the experimental data in the high S_w region. Also the stagnation of saturation before equilibrium is reached is not simulated by the models. The initial saturation of the C-155 layer estimated from $P_c(S)$ curve is different than its measured value during the dynamic test. This discrepancy can be explained by the large uncertainty of the statically measured C-155 water saturation at an air pressure of 4500 Pa (see Fig. 11a).

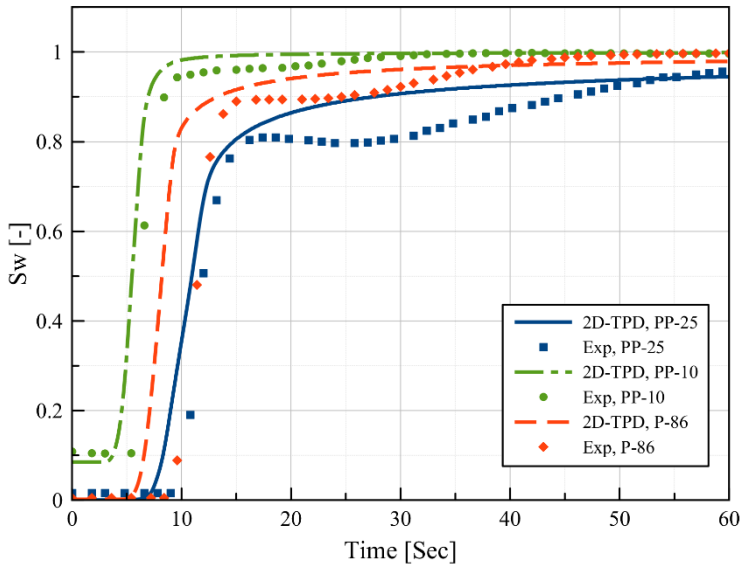

Figure 17. 2D-TPD modeling results of dynamic inflow for the layers with surficial bonding patterns: P-86, PP-25 and PP-10.

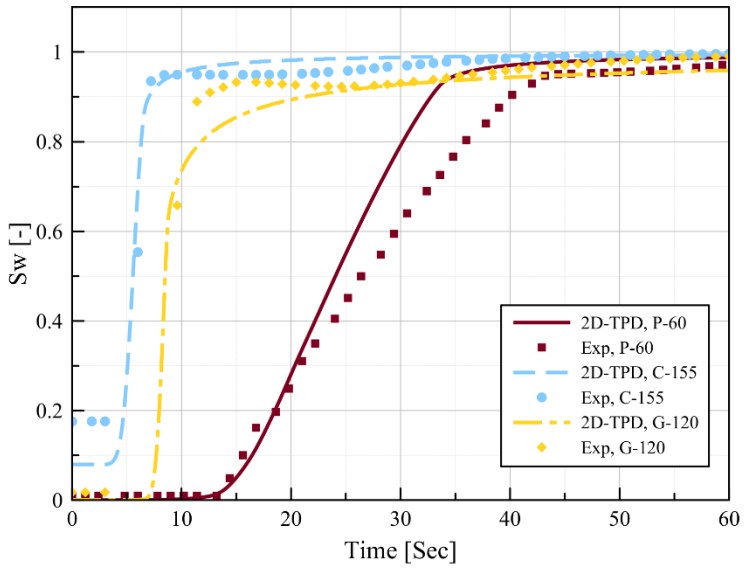

Figure 18. 2D-TPD modeling results of dynamic inflow for the layers without surficial bonding patterns: P-60, G-120 and C-155.

Fig. 19 illustrates the effect of dynamic capillarity. In this sensitivity analysis three different τ values are used for each of the six layers. A simulation is done with a τ value of 0 Pa.s, 1000 Pa.s, and a value that is based on Stauffer (1978) (Table 6).

Table 6. Stauffer (1978) based τ values for all six layers.

Layer material	Stauffer (1978) based τ value [Pa.s]
P-86	1788
PP-25	1045
PP-10	8897
P-60	3
G-120	366278
C-155	8815

Including dynamic capillarity leads to a more gentle slope of the wetting curve (Fig.19). The initial moment at which wetting of the sample starts, is however not affected by dynamic capillarity. The τ values that are based on the Stauffer (1978) formula do not yield satisfactory results, especially for the simulations with relatively high τ values (PP-10, G-120, C-155).

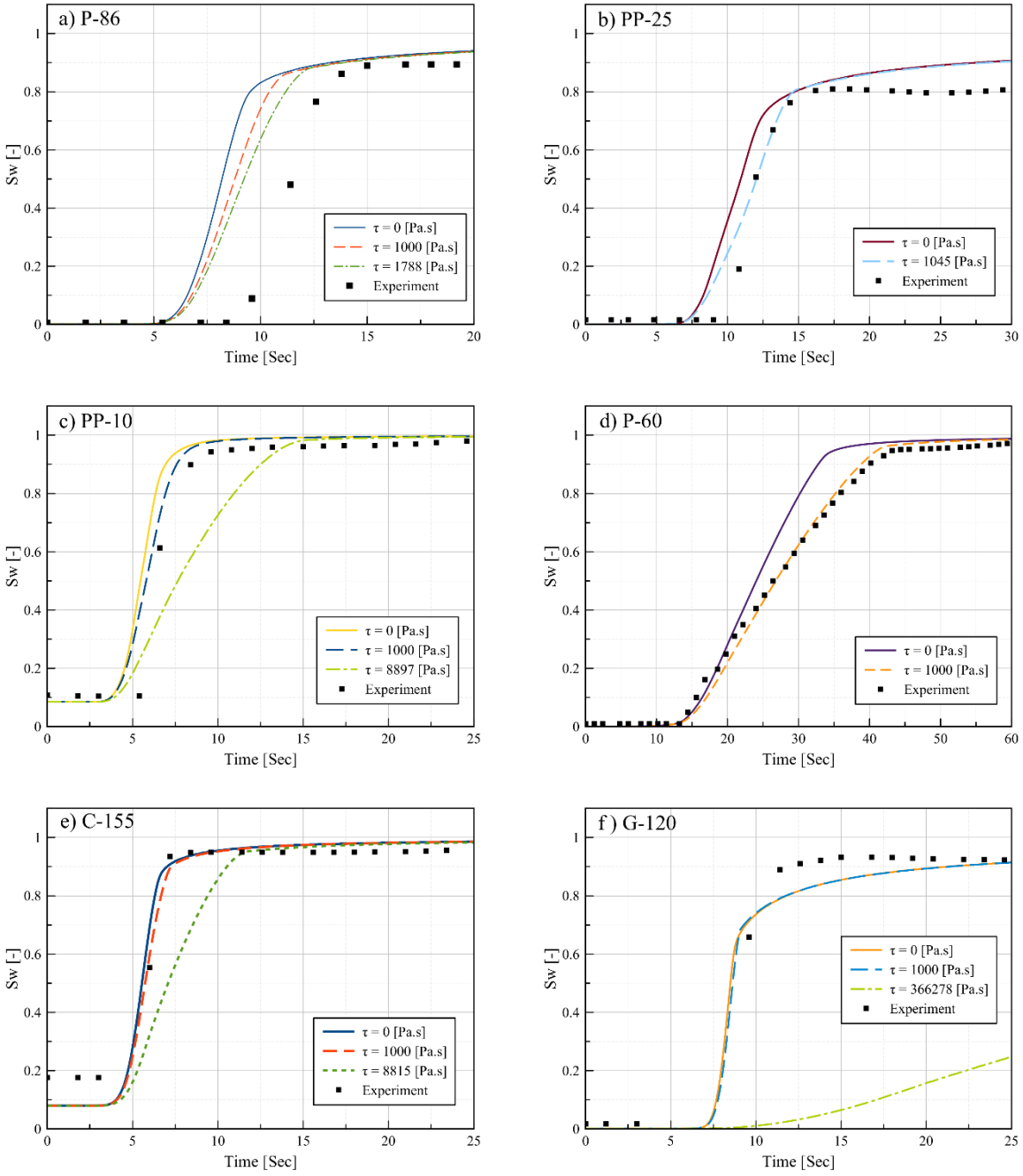

Figure 19. Effect of dynamic capillarity on predicted water saturation curves of all six materials: a) P-86, b) PP-25, c) PP-10, d) P-60, e) G-120, f) C-155

Fig. 20 illustrates the effect of varying relative permeability functions at low air and water saturations on simulated water saturation curves for the PP-25 and PP-10 layer. These are two layers for which a time delay between pressure drop and the initial moment of sample wetting is observed. The results show that the modified relative water permeability leads to a slight time delay before wetting of the surface occurs. The modified relative air permeability leads to a more satisfactory results in the upper part of the curve, due to the enhanced air entrapment in the center of the sample. In contrast to the layers with surficial bonding patterns, there is no need for modification of the relative permeability functions of Eqs. (13 and 14) for layers without surficial bonding patterns (Fig. 17). This suggests another possible explanation for the time shift between simulation and experimental results, namely that this discrepancy has more of a interlayer contact dependent origin instead of a purely saturation dependent origin.

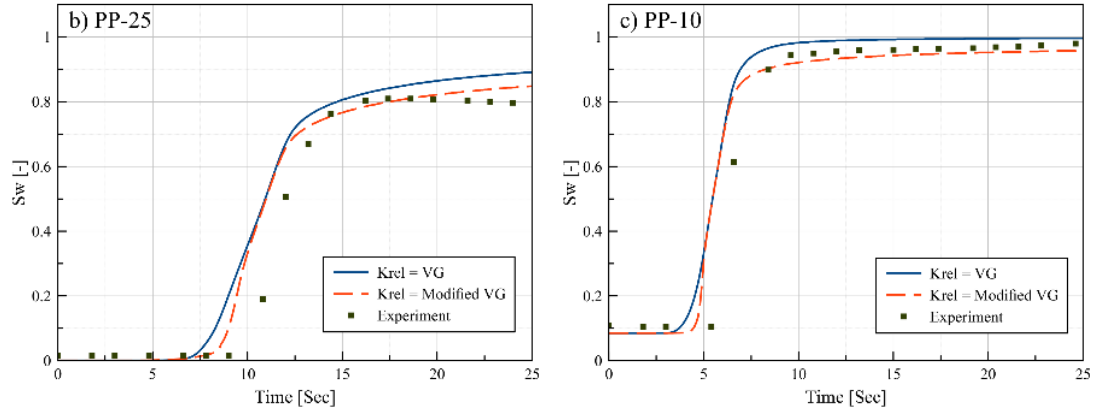

Figure 20. Effect of different relative permeability functions at low water and air saturations on predicted water saturation curves of layers with physical bonding patterns: a) P-86, b) P-25, c) P-10.

Finally, material characterizations of all six nonwoven fabric layers are provided based on the best fit of experimental data points. Best fits for C-155 and G-120 are those obtained from the 2D-TPD model without any further modifications (Fig. 18). For P-60, the exact time of initial wetting is accurately simulated but the slope of water saturation curve can be matched best by including a dynamic capillarity effect with τ =1000 Pa.s. For all the layers with a surficial bonding pattern, best fits of the experimental data are achieved after modification of the relative permeability function and consideration of dynamic capillarity (Fig. 21).

The use of many fitting parameters makes the physical sense of the used modelling approach disputable. Also, the fitting process itself, is inconsistent for different fibrous materials. For example, the P-60 layer simulation fits satisfactory after adjustment of the τ value only, whereas simulations of other layers (P-86, P-25, P-10) fit satisfactory after adjustment of the τ, k_r^w, and k_r^wparameters. The adjustment of the relative permeability function is arbitrary. Also the model seems to be highly dependent on initial water saturation. Lastly, the effect of interlayer processes are not explicitly included in the models.

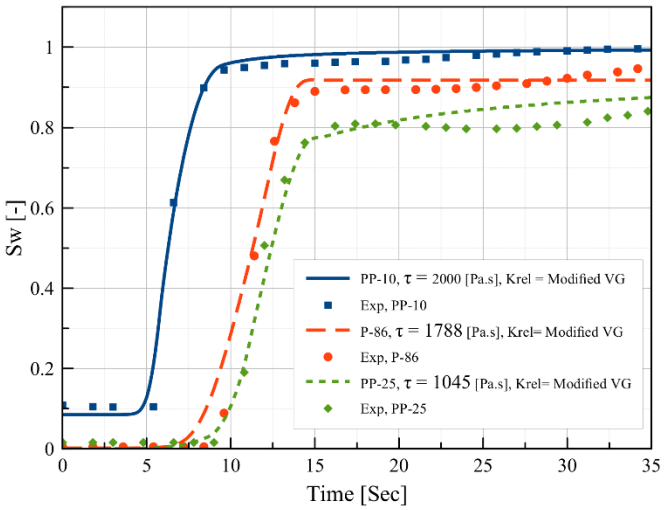

Figure 21. Best 2D-TPD fits of water saturation evolution over time for materials with surficial bonding patterns, after inclusion of tau coefficient and modification of relative permeability function at low saturation.

3.3 Dynamic inflow modeling results with Reduced continua model (RCM)

3.3.1 Model evaluation stage based on P-86

The RCM results are compared to the continuum-scale 2D-TPD model results (Fig. 22). This preliminary RCM model version includes the same saturation function as used by Qin & Hassanizadeh (2015), given in Eq. 26. A value of 3 is implemented for $y1$ and $y2$.

Results of the RCM models are similar to the equivalent continuum-scale models. Results of the 1D-RCM(TP), 1D-RCM(SP), and 2D-RCM(SP) are almost identical. The 2D-RCM(TP) simulates different results because vertical flow component plays a significant role, as was the case with the 2D-TPD model. There is a small discrepancy between these preliminary 2D-RCM(TP) result and the equivalent 2D-TPD continuum-scale model (Fig. 22). This is caused by the use of the f factor to account for relative water permeability during water transport through the interface, instead of VG based relative permeability.

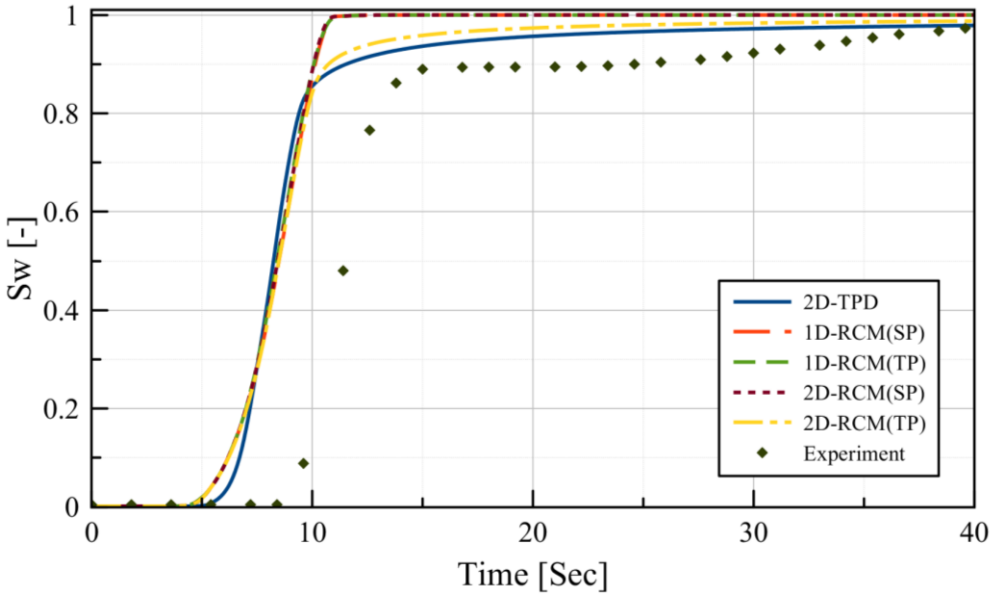

Figure 22. Preliminary P-86 simulation results of four RCM models compared to 2D-TPD results.

3.3.2 Simulations of all six fibrous layers

Based on the results in Fig. 22, the experiments of all fabric layers are simulated with the 2D-RCM(TP). The 2D-RCM(TP) results with Eq. (26) as saturation function still show the discrepancy of initial wetting time for the fabric layers with surficial bonding patterns, compared to the experimental data (Fig. 22). The continuum-scale models illustrated that the modification of the VG based relative permeability functions at these low saturations yields a better fit of the experimental results. In the RCM model it is the mass transfer coefficient that affects the transfer of water from the membrane to the fabric. More specifically, it is the $f(S_f^w, S_m^w)$ term that represents the relative permeability for liquid water transport through the interface. Therefore this term is investigated in more detail.

The original saturation function introduced by Qin & Hassanizadeh (2015) (Eq. 26) was used for the simulation of flow between two layers of unsaturated media, hence the range of $f(S_f^w, S_m^w)$ was a range between 0 and 1. Because the membrane is always fully saturated in this study, this $f(S_f^w, S_m^w)$ term has a minimum value of 0.5. This term is therefore not suitable to simulate the resistance to water flow in the sample under low water saturation conditions. The saturation functions of Eqs. (27 and 28) where examined.

In the saturation functions of Eqs. (26, 27, and 28), as well as in all continuum-scale models, simulation results are highly dependent on the initial water saturation. This is true because the initial water

saturation determines the initial relative water permeability. This initial saturation dependency does not make physical sense, since connecting path ways between the water phases in the sample are not yet present at these low initial water saturations. As indicated by the pore scale analyses results using the GeoDict® program, effective water permeability is actually zero. Therefore one could say that at these low water saturations the use of any effective permeability dependent equation to quantify the transport of water between two layers is physically incorrect. In Eq. (29) we therefore consider a constant saturation independent f factor until a certain threshold saturation is reached. After this saturation is reached, the original saturation function of Eq. (26) was applied.

The fitting results of the RCM simulations with three different saturation functions of Eqs. (27, 28, and 29) are included in Fig. 23. Simulation results of the layers with a surficial bonding pattern (P-86, P-25, P-10) fit satisfactory to the experimental results if a relatively high power function is used for the saturation function of Eq. (27). On the other hand, the layers without a surficial bonding pattern (P-60, G-120, C-155) fit well with a lower power function.

Fitting with the saturation function of Eq. (28) also results in a contradiction between layers with and without a surficial bonding pattern. For layers without a surficial bonding pattern, the fitting is not sensitive to any of the parameters, as long as A is relatively high, leading to a high f at low initial saturations. The layers with a surficial bonding pattern fit well with a low A value and high B value. The A parameter is the most influential fitting parameter because it determined the initial value of f.

The need of a lower initial f value for the layers with a surficial bonding pattern is also confirmed by the saturation function of Eq. (29). Low initial Z values are required for layers with a surficial bonding pattern, whereas high initial Z values are required for layers without a surficial bonding pattern. Arbitrary q values had to be applied in order to fit the experimental data satisfactory.

Overall, all three applied saturation functions yield satisfactory results. However, one could question the use of many fitting parameters, especially since they do not have a physical basis. Also, this modelling procedure is arbitrary to the exact saturation function that is used.

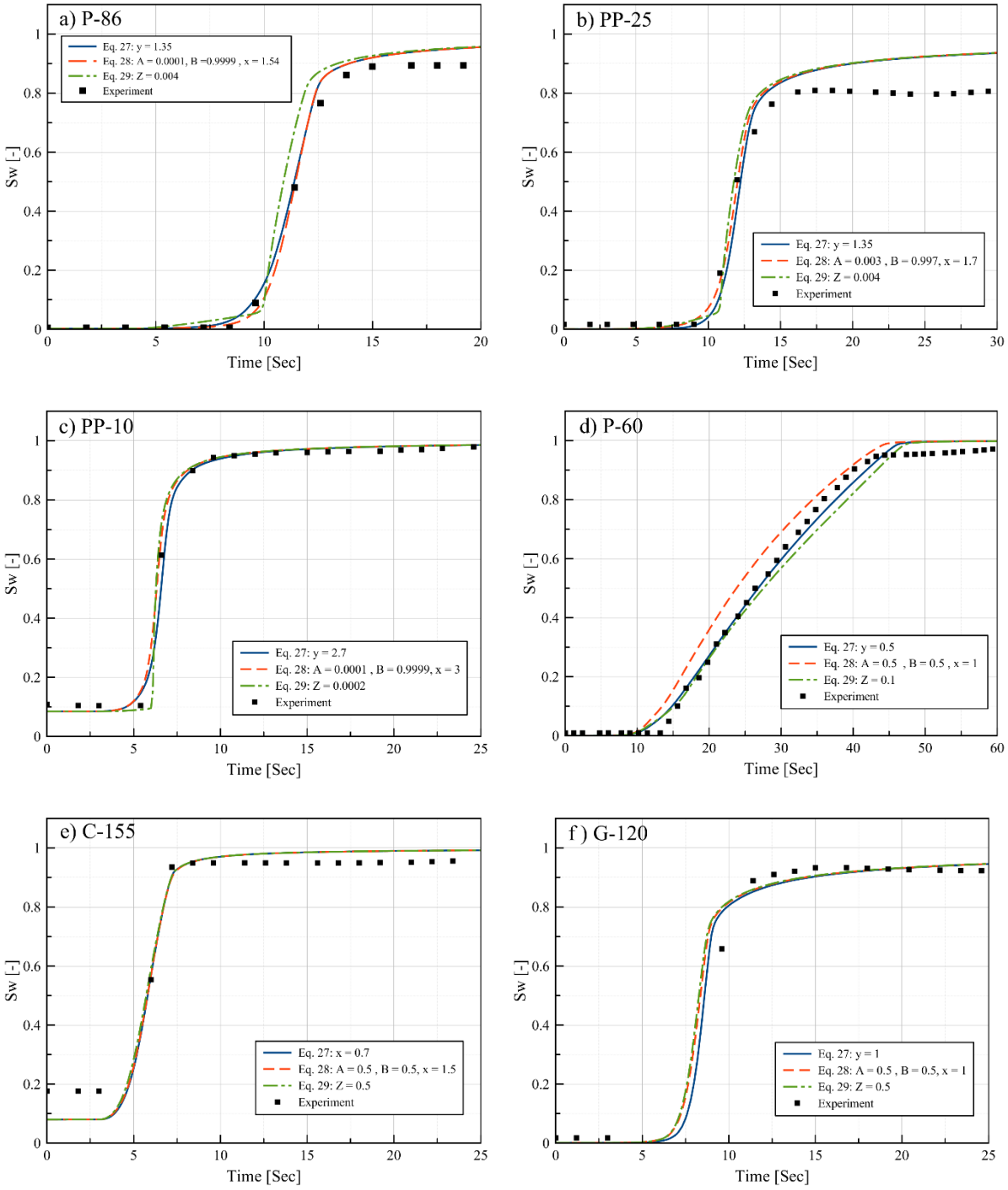

Figure 23. 2D-RCM(TP) results of all six layer after using three different saturation functions (Eqs. 27, 28, and 29).

The 2D-RCM(TP) model with exchange coefficient of Eq. (30) does take interlayer space effects into account. In this approach, it is assumed that the flux between layers depends on the water transfer rate in the connected pores of interlayer space, and therefore on the quality of contact between two layers. The λ factor is used to specify the quality of contact in the interlayer space. Before water reaches to a residual saturation of a sample layer, connected pathways are not created in the sample, and the flux only depends on the interface properties. Constant coefficient C is used in the exchange coefficient term before a residual saturation is reached. Since this initial exchange coefficient should only depend on interlayer properties (λ) and not on hydraulic properties within the layer itself, C should be the same for all materials. Trial and error simulations indicated that simulations with C is equal to 3.35e-5 [m s^{-1}]

yield good results. After reaching the residual saturation threshold, the harmonic mean of relative permeabilities determines the exchange between the two layers.

Results for layers without a surficial bonding pattern are given in Fig. 24. The λ coefficient is assumed to be 1 for these layers because the membrane and the fabric layer are almost perfectly connected due to the applied overburden pressure. Very close agreement is reached between 2D-RCM(TP) results and measured saturation data points of P-60, C-155 and G-120. Simulations of these layers with lower λ values yield results that are not satisfactory with experimental data.

Fig. 25 indicates that layers with a surficial bonding pattern require a lower λ value in order to account the imperfect contact between a fabric layer and the membrane. Values of λ is equal to 0.23 and 0.18 are needed to fit the experimental results for P-86 and PP-25 respectively, while an even lower value of 0.08 is required for PP-10. The interlayer pore space effect is more pronounced in these layers due to the fact that large pores are present in the interstices of fabric sample and membrane.

The 2D-RCM(TP) results of PP-10, given in Fig. 25 perfectly match with measured data for whole saturation range when lambda is assumed to be 0.08. For PP-25 and P-86 materials, very good agreement is reached for saturations up to 0.8 by reducing lambda factor. Still, at high water saturations above 0.8, the two step bumpy nature of the experimental data is not fitted correctly by the RCM.

The RCM results confirm that the inconsistency in simulated dynamic water saturation curves of a group of 6 nonwoven fibrous layers corresponds to interlayer effects between sample and membrane. Only one fitting parameter λ, that has a sound physical basis, is needed in this RCM approach to simulate the imbibition of any material.

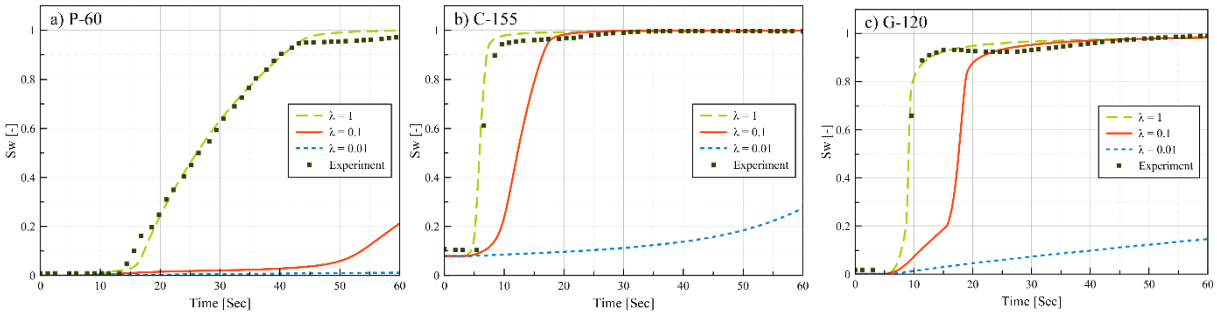

Figure 24. Equations 30 and 31 based 2D-RCM(TP) results of dynamic inflow for three fabric layers without a surficial bonding pattern.

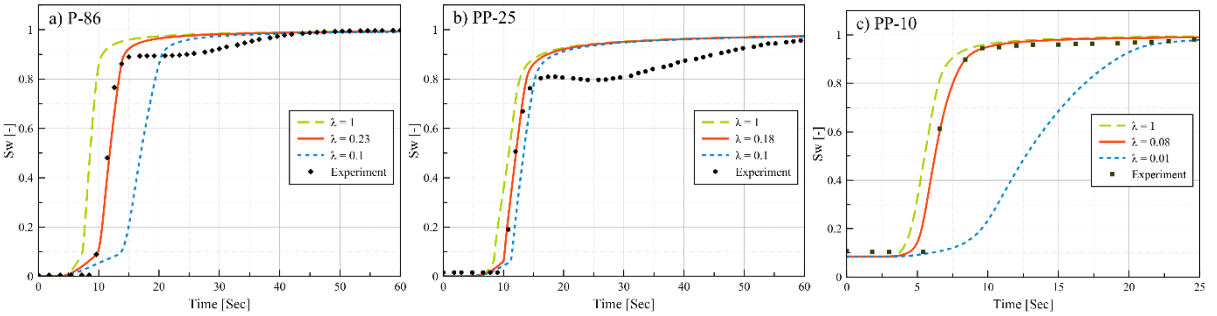

Figure 25. Equations 30 and 31 based 2D-RCM(TP) results of dynamic inflow for three fabric layers with a surficial bonding pattern.

3.4 Dynamic outflow experiments

Fig. 26 show results of dynamic outflow experiments. The transient air pressure data and water saturation are given for each material. The experimental data for PP-10, PP-25, P-86, P-60, and C-155, after a pressure increase to 4500 Pa, are plotted in Fig. 26a. The experimental out flow results of G-120, after increasing the air pressure to both 10000 Pa and 20000 Pa, are given in Fig. 26b. The equilibrium water saturations at these pressures are 0.67 and 0.31 respectively.

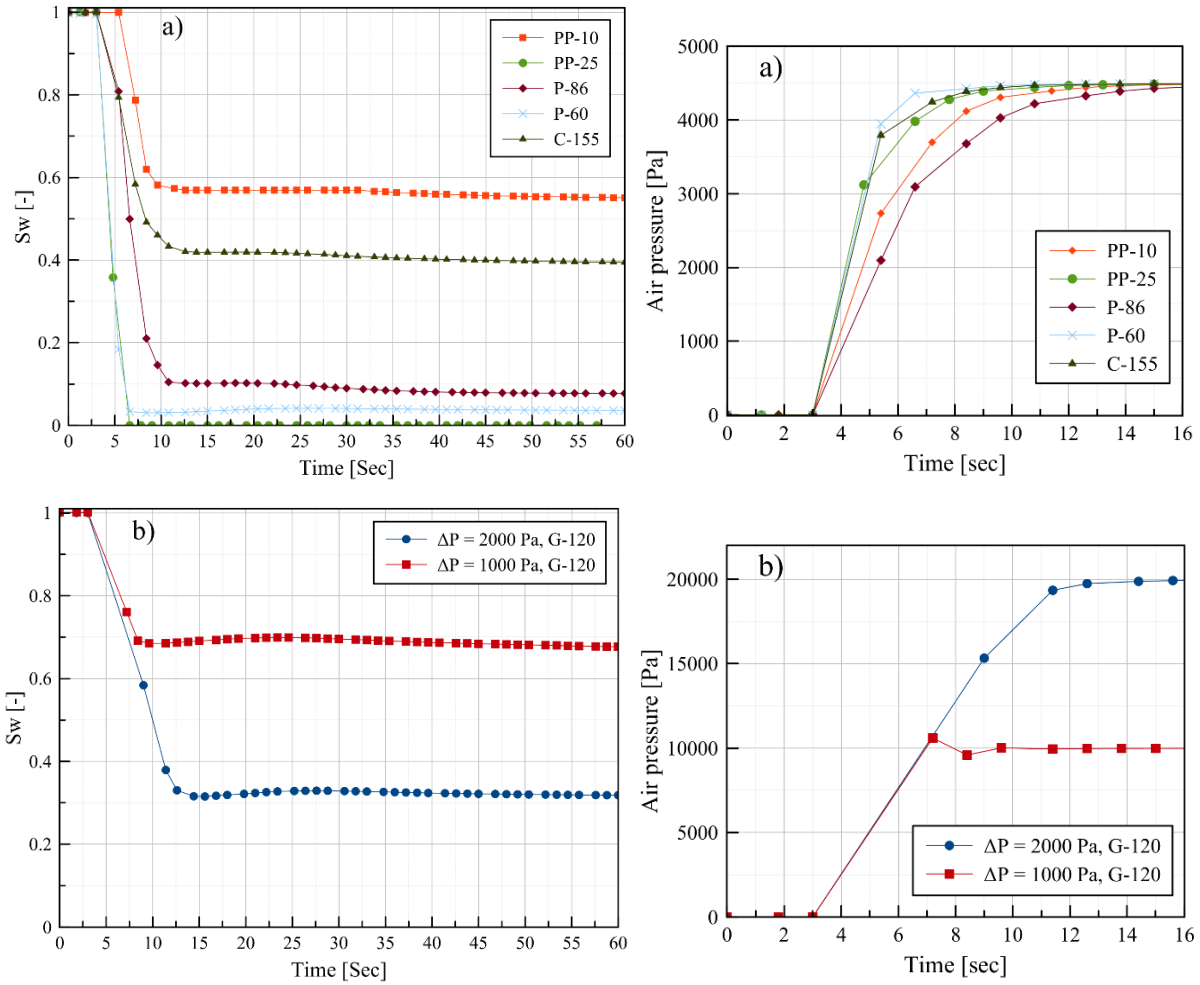

Figure 26. Results of dynamic outflow experiments for; a) PP-10, PP-25, P-86, P-60, C-155 when exposed to a pressure drop of 4500 Pa, and b) G-120 when exposed to pressure drop of 2000 and 1000 Pa.

3.5 Dynamic outflow modeling results with two-phase flow model and RCM

Dynamic outflow simulation results, with both the 2D-TPD model and 2D-RCM(TP), are given in Fig. 27. Both models can predict the experimental data satisfactorily for all layers. The experimental data can be fitted satisfactory when the same λ values as used in inflow simulations are applied. This implies that a λ value of 1 is used for the G-120, P-60, and C-155 simulations, while the λ value was set to 0.08 for PP-10, 0.18 for PP-25 and 0.23 for P-86. The sensitivity to λ is also illustrated in Fig. 27. Implementation of a λ value of 1 results in saturation curves that are practically equal to the 2D-TPD model results. This shows that the 2D-RCM(TP) model is an accurate way of simulating flow, despite the reduction of the vertical dimension of the model domain. Also, the computational effort is reduced significantly. Slightly better results are obtained when a lambda value of 0.23 is applied for the P-86 simulation (Fig. 27a). The G-120 simulation do not fit experimental results satisfactory. This is explained by the inaccurate VG fit (Fig. 11b). Overall the VG fits of the drainage data are less accurate than the VG fits of the imbibition data. This can also partly explain the slight mismatch of the PP- 10, P-60, and C-155 simulations with the experimental data. The results indicate that application the same

λ value for both inflow and outflow simulations is the best approach for modeling dynamic unsaturated flow in the thin porous layers.

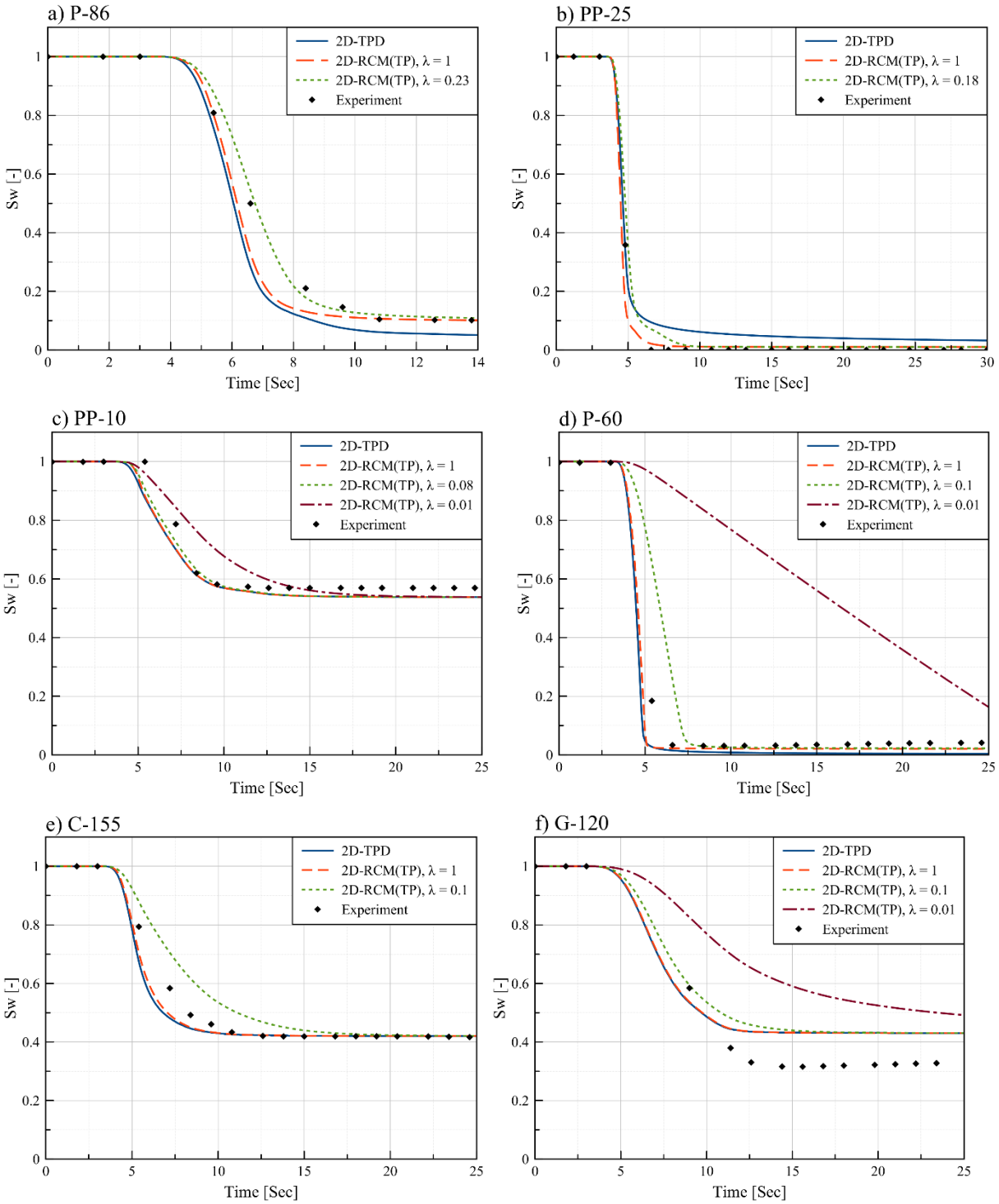

Figure 27. Equations 30 and 31 based 2D-RCM(TP) simulation results and 2D-TPD simulation results of dynamic outflow for all six layers.

3.6 Discussion and relation to future research

Modeling efforts in this study have indicated that the RCM is very well capable of predicting dynamic average saturation evolution of all materials by consideration of a contact quality parameter in the mass exchange coefficient between membrane and fabric sample. This contact quality parameter, λ, imposes a limitation to the water transfer rate. This makes sense, since a lower contact quality between two layers leads to fewer connected pores in the interlayer space, and therefore a lower maximum water transfer rate compared to two layers in which connecting pores occur over the entire contact surface. In line with results from (Tavangarrad, 2018), the RCM results are found to be in good agreement with the experimental results without adding a dynamic capillarity term (τ).

The inclusion of the *C* parameter, which determines the mass transfer before the residual saturation is reached in the layer, accounts for the buildup of saturation in the interlayer pore space and in the sample layer. It is assumed that before residual saturation was reached, connected pathways are not created in the sample, and the interlayer flux only depends on the interface properties. Therefore the *C* parameter must be constant in this experimental setup. It can be discussed that the hydraulic properties of the membrane layer determine the *C* parameter value. Two different membranes should be used to evaluate this hypothesis.

It should be noted that this study specifically focusses on the simulation of fluid flow through two layers in which one of the layers is fully saturated. Under certain circumstances, where both layers are initially unsaturated, another factor comes into play. In these conditions water saturation must first build in the donating layer and interfacial pore space before connecting path ways with the receiving layer can be formed. One should consider how the findings of this study could be applied in such circumstances. A third circumstantial condition, taking into account the threshold saturation of the water donating layer, should be added to the mass exchange coefficient of Eq. (30), analogous to (Tavangarrad, 2019). Before this threshold saturation is reached, the interlayer mass transfer is zero. If the *C* parameter is in fact a function of hydraulic properties of the water donating layer, this parameter may become a function of saturation of this donating layer.

In this study the contact quality parameter, λ, was found through inverse modelling. For practical application of this modeling method, it is desired to derive the λ value from physical characteristics of the considered fibrous layer. In this study it was observed that the bonding pattern in some layers cause large pores in the interstices of sample and membrane and therefore lead to a poorer contact quality and lower λ value. Other experiments, in which the overburden pressure was not applied, showed that the looser contact between the membrane and sample layer leads to a lower mass transfer rate. Future research could aim for an empirical relation that describes λ as a function of surface roughness characteristics of fibrous layer, pressure of contact, and other possible parameters.

4 Conclusion

In this study quasi-static and dynamic inflow and outflow experiments for a group of six nonwoven fibrous materials are performed using the autoporosimetry technique. $P_c(S)$ curves are constructed form the measured quasi-static data points. The $P_c(S)$ curves are fitted with the Van Genuchten (1980) equation. The resulting fitting parameters were used as an input for modeling dynamic experiments. Dynamic inflow and outflow experiments were conducted by implementing a sudden air pressure change in about 15 seconds. This results in the rapid infiltration in- or drainage of the sample.

A total of eight individual models were evaluated. Four continuum-scale model are constructed: a 1D Richards model (1D-R), a 1D Darcy-based two-phase flow model (1D-TPD), a 2-D axisymmetric Richards model (2D-R), a 2-D axisymmetric Darcy-based two-phase flow model (2D-TPD). Also, four different types of Reduced Continua Models (a new type of model where all properties of thin porous material are averaged in the through-plane direction) are constructed: a 1D-RCM(SP), a 1D-RCM(TP), a 2D-RCM(SP), and 2D-RCM(TP). The 2D-RCM(TP) proved to be best suitable for the simulation of the performed experiments.

The 2D-TPD model approach approximates the measured saturation inflow data satisfactorily for three nonwoven fabric layers without a surficial bonding pattern. However, for three fibrous layers whose surface structure has been altered as a consequence of a bonding process, experimental data shows a time delay of the initial moment of wetting of the surface when compared to the numerical result of the 2D-TPD model. The inclusion of a dynamic capillarity term, cannot explain this discrepancy with experimental results. In comparison to this modeling approach, the 2D-RCM(TP) accurately predicts average saturation evolution of all materials after inclusion of a contact quality parameter in the mass exchange coefficient between membrane and sample..

The outflow simulation results are close to experimental data in both modeling approaches. Slight discrepancies between simulation and experimental results can be allocated to inaccuracies in the VG fits. Also, slightly better agreement with experimental results are achieved with RCM when the same contact quality parameter value as used for the inflow simulations, is implemented. The RCM is a thermodynamically based, robust, and powerful technique for the prediction of unsaturated dynamic fluid flow in thin porous media. Not only is this new technique computationally efficient and preserves REV concept for thin porous layers, but also the effect of interlayer pore space between two neighboring layers in a stack of multiple thin layers can be taken onto account, using the mass exchange coefficient.

5 References

Ashari, A., & Tafreshi, H. V. (2009). General capillary pressure and relative permeability expressions for through-plane fluid transport in thin fibrous sheets. *Colloids and Surfaces A: Physicochemical and Engineering Aspects*, *346*(1-3), 114-122.

Aslannejad, H., & Hassanizadeh, S. M. (2017). Study of hydraulic properties of uncoated paper: image analysis and pore-scale modeling. *Transport in Porous Media*, *120*(1), 67-81.

Beliaev, A. Y., & Hassanizadeh, S. M. (2001). A theoretical model of hysteresis and dynamic effects in the capillary relation for two-phase flow in porous media. *Transport in Porous media*, *43*(3), 487-510.

Van Genuchten, M. T. (1980). A closed-form equation for predicting the hydraulic conductivity of unsaturated soils 1. *Soil science society of America journal*, *44*(5), 892-898.

Gostick, J. T., Fowler, M. W., Ioannidis, M. A., Pritzker, M. D., Volfkovich, Y. M., & Sakars, A. (2006). Capillary pressure and hydrophilic porosity in gas diffusion layers for polymer electrolyte fuel cells. *Journal of power sources*, *156*(2), 375-387.

Hassanizadeh, S. M., Celia, M. A., & Dahle, H. K. (2002). Dynamic effect in the capillary pressure–saturation relationship and its impacts on unsaturated flow. *Vadose Zone Journal*, *1*(1), 38-57.

Hassanizadeh, S. M., & Gray, W. G. (1990). Mechanics and thermodynamics of multiphase flow in porous media including interphase boundaries. *Advances in water resources*, *13*(4), 169-186.

Hassanizadeh, S. M., & Gray, W. G. (1993). Thermodynamic basis of capillary pressure in porous media. *Water resources research*, *29*(10), 3389-3405.

Jaganathan, S., Tafreshi, H. V., & Pourdeyhimi, B. (2009). A realistic modeling of fluid infiltration in thin fibrous sheets. *Journal of Applied Physics*, *105*(11), 113522.

Landeryou, M., Eames, I., & Cottenden, A. (2005). Infiltration into inclined fibrous sheets. *Journal of Fluid Mechanics*, *529*, 173-193.

Miller, B., & Tyomkin, I. (1994). Liquid porosimetry: new methodology and applications. *Journal of colloid and interface science*, *162*(1), 163-170.

Mirzaei, M., & Das, D. B. (2007). Dynamic effects in capillary pressure–saturations relationships for two-phase flow in 3D porous media: Implications of micro-heterogeneities. *Chemical engineering science*, *62*(7), 1927-1947.

Nguyen, T. V., Lin, G., Ohn, H., & Wang, X. (2008). Measurement of capillary pressure property of gas diffusion media used in proton exchange membrane fuel cells. *Electrochemical and Solid-State Letters*, *11*(8), B127-B131.

Prat, M., Agaësse, T. (2015). Thin porous media. In: Vafai, K. (ed.) Handbook of Porous Media (Chapter 4), 3rd edn. Taylor & Francis, London

Qin, C. Z., & Hassanizadeh, S. M. (2014). Multiphase flow through multilayers of thin porous media: General balance equations and constitutive relationships for a solid–gas–liquid three-phase system. *International Journal of Heat and Mass Transfer*, *70*, 693-708.

Qin, C. Z., & Hassanizadeh, S. M. (2015). A new approach to modelling water flooding in a polymer electrolyte fuel cell. *international journal of hydrogen energy*, *40*(8), 3348-3358.

Qin, C., Rensink, D., Fell, S., & Hassanizadeh, S. M. (2012). Two-phase flow modeling for the cathode side of a polymer electrolyte fuel cell. *Journal of power sources*, *197*, 136-144.

Rebai, M., & Prat, M. (2009). Scale effect and two-phase flow in a thin hydrophobic porous layer. Application to water transport in gas diffusion layers of proton exchange membrane fuel

cells. *Journal of Power Sources*, *192*(2), 534-543.

Stauffer, F. (1978, August). Time dependence of the relations between capillary pressure, water content and conductivity during drainage of porous media. In *IAHR symposium on scale effects in porous media, Thessaloniki, Greece* (Vol. 29, pp. 3-35).

Szymkiewicz, A. (2013). Mathematical models of flow in porous media. In *Modelling Water Flow in Unsaturated Porous Media*(pp. 9-47). Springer, Berlin, Heidelberg.

Tavangarrad, A. H., Mohebbi, B., Hassanizadeh, S. M., Rosati, R., Claussen, J., & Blümich, B. (2018). Continuum-Scale Modeling of Liquid Redistribution in a Stack of Thin Hydrophilic Fibrous Layers. *Transport in Porous Media*, *122*(1), 203-219.

Tavangarrad, A.H.: Experimental and computational study of unsaturated flow in a stack of thin layers, Application to non-woven hygiene products. *Phd thesis book*, ISBN:978-90-6266-526-6 (2019).

Ye, Q., & Van Nguyen, T. (2007). Three-dimensional simulation of liquid water distribution in a PEMFC with experimentally measured capillary functions. *Journal of the Electrochemical Society*, *154*(12), B1242-B1251.

Appendix

Appendix 1

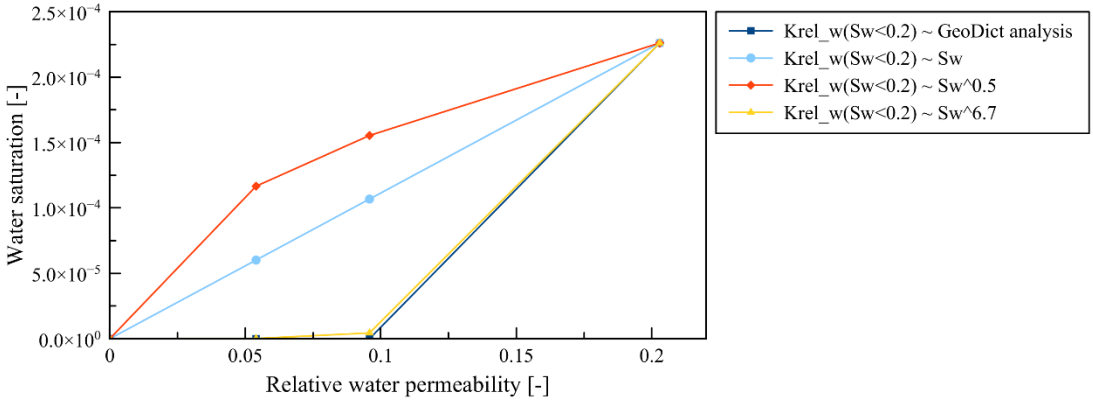

Figure A1a. Three methods of replacing the zero values of the relative water permeability pore scale analysis of Table 5.

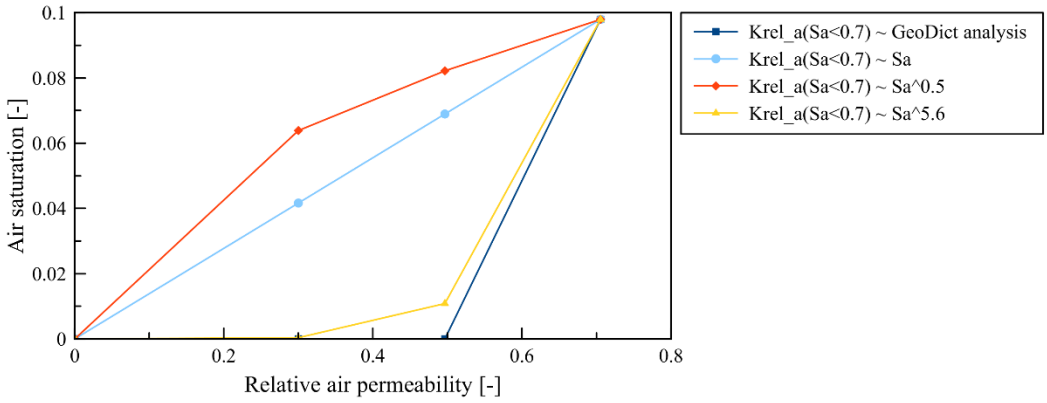

Figure A1b. Three methods of replacing the zero values of the relative air permeability pore scale analysis of Table 5.

Appendix 2

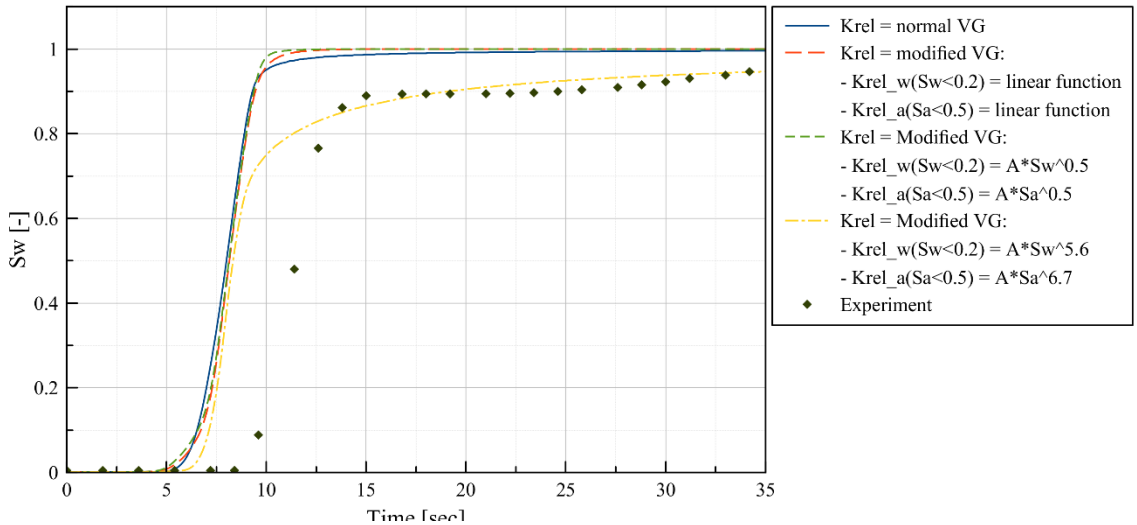

Figure A2. Saturation evaluation curves of the 2D-TPD model. Comparison of four different relative permeability functions.

Appendix 3

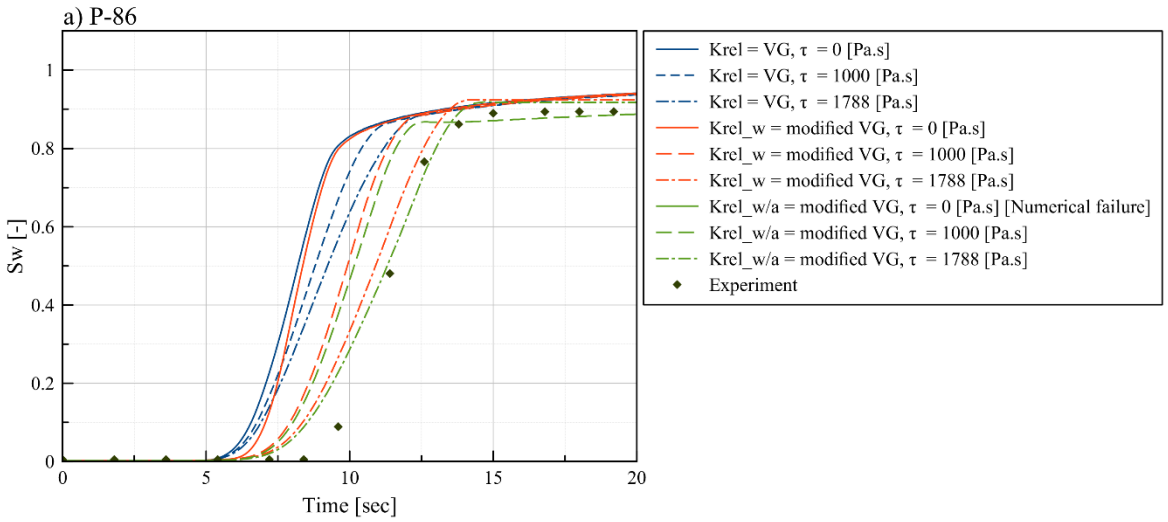

Figure A3a. 2D-TPD simulations for P-86

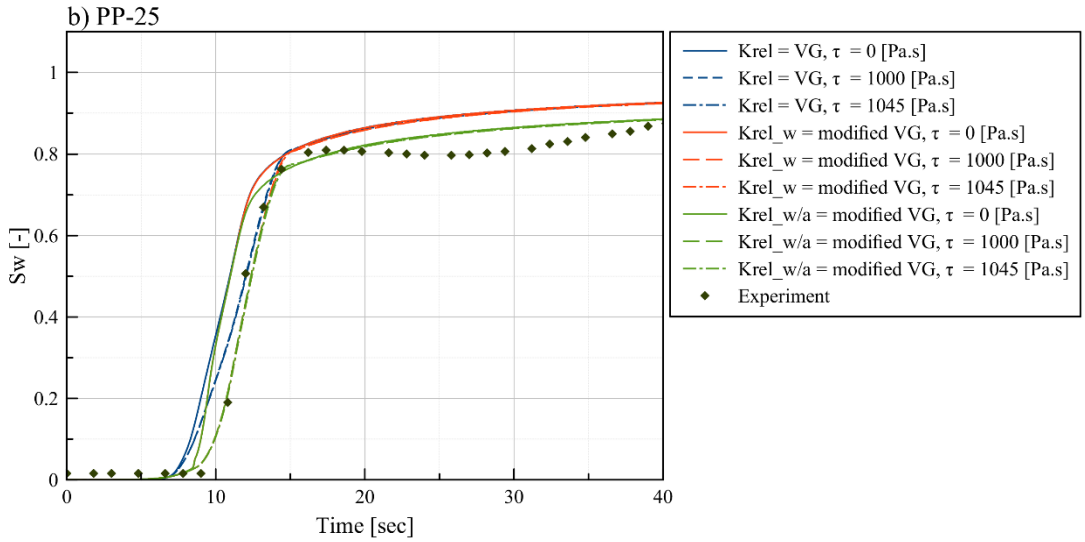

Figure A3b. 2D-TPD simulations for PP-25

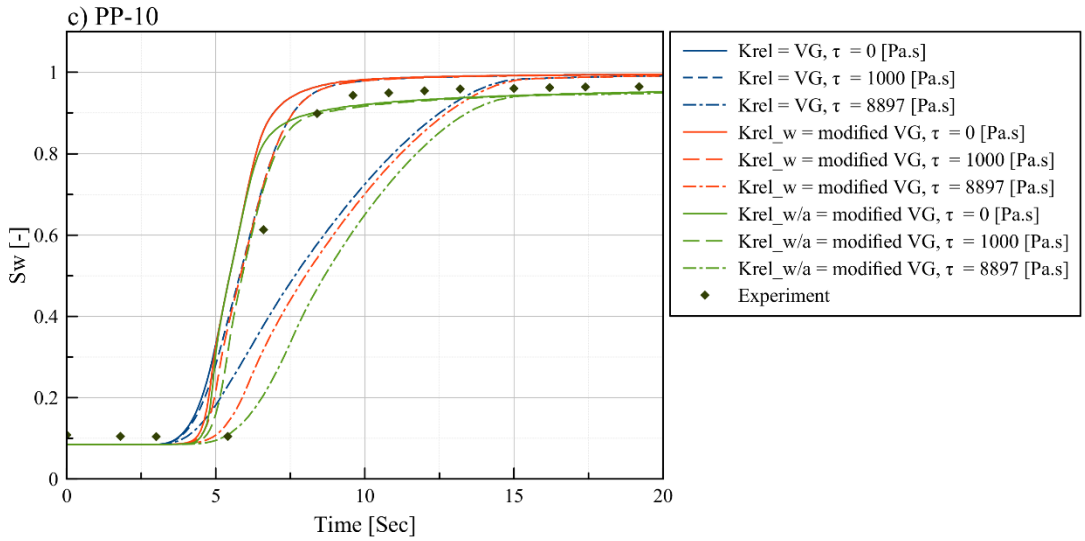

Figure A3c. 2D-TPD simulations for PP-10

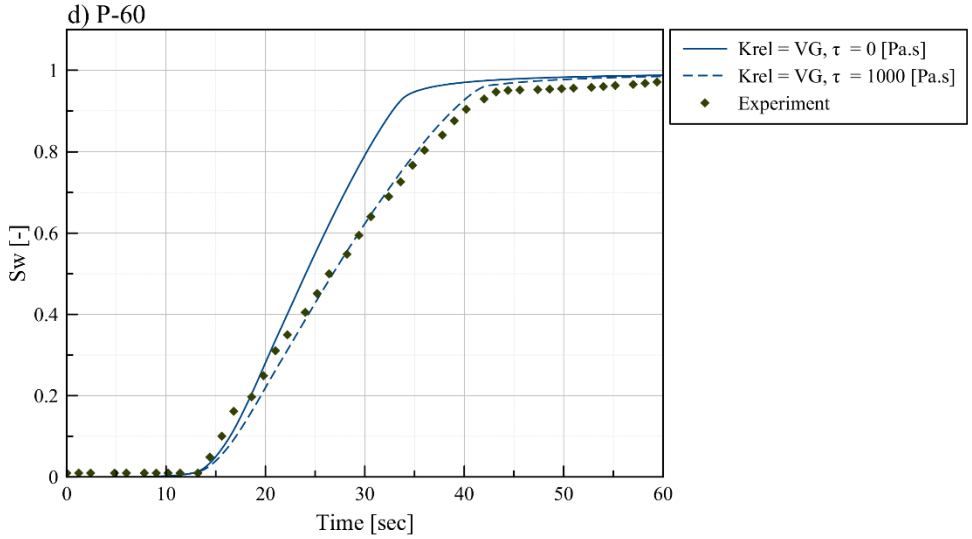

Figure A3d. 2D-TPD simulations for P-60.

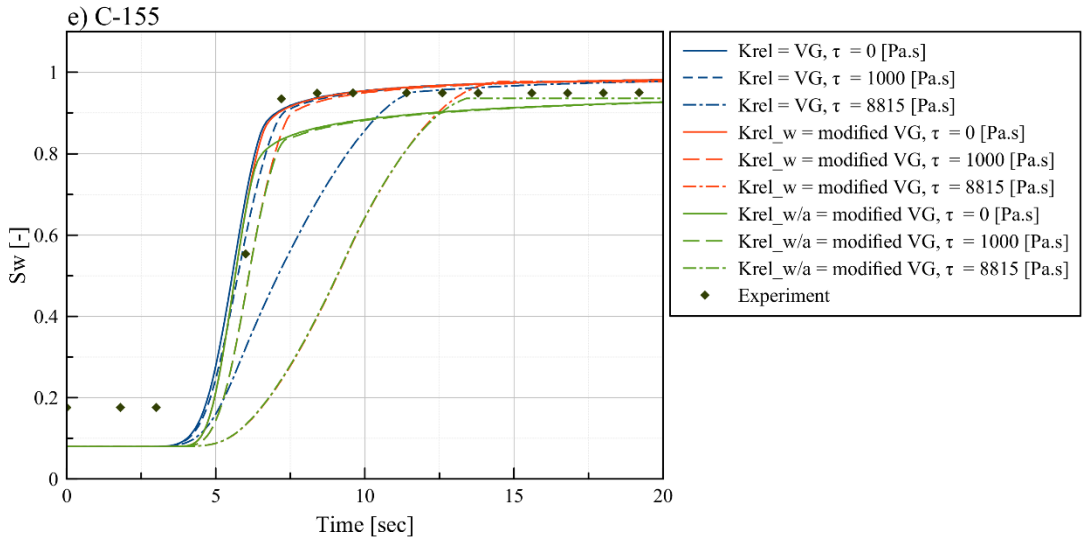

Figure A3e. 2D-TPD simulations for C-155

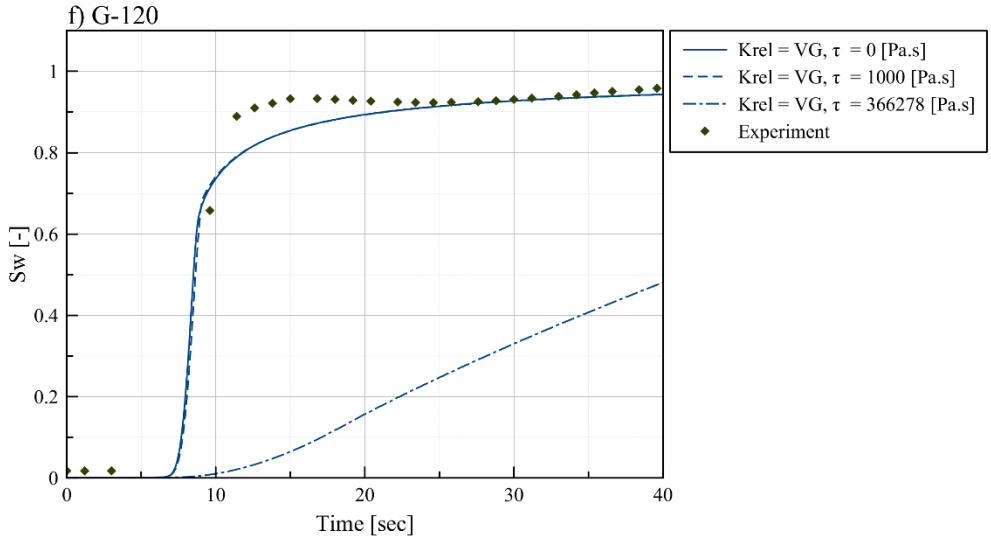

Figure A3f. 2D-TPD simulations for G-120